Reply to the reviewer comments on the manuscript

Radiative transfer simulations and observations of infrared spectra in the presence of polar stratospheric clouds: Detection and discrimination of cloud types

by C.Kalicinsky et al.

We thank the reviewers for their helpful comments and recommendations. In the following, we discuss the issues addressed by the reviewers and explain our opinions and the modifications of our manuscript.
We enumerate the comments and repeat them in bold face. The modifications of the manuscript are displayed in the marked-up manuscript version as colored text. Deleted parts are shown in red and new or modified text parts in blue.

1 Comments Reviewer 1

General comments
Based on radiative transfer simulations, the authors present a method to detect and discriminate PSCs in airborne CRISTA-NF observations. NAT and ice are identified by using their characteristic spectral patterns. Detected PSCs, which do not show these signatures, are classified as STS. Assuming spectral characteristics of spherical particles, NAT PSCs are sub-grouped into small NAT (median r≤1.0μm), medium-sized NAT (median r=1.5μm – 4.0μm) and large NAT (median r≥3.5μm). Furthermore, a new method to detect the bottom altitude of non-opaque clouds is introduced. Application of the proposed methods to CRISTA-NF data is presented for one flight during the RECONCILE field campaign.
The presented study is interesting for PSC-related research, since aspects of PSC detection and classification are investigated in further detail and extended. The CRISTA-NF observations provide another interesting data set in the winter 2009/10, which was characterised by wide-spread PSC occurrence. The proposed approach to distinguish between different size classes of NAT particles might have potential to extend PSC classification using satellite instruments. However, the presented size classification is elaborated using model simulations only. Direct and detailed comparisons with observed spectra are not presented. Only spherical NAT particles are taken into account, while previous studies suggest that particle shape is an important issue. Comparisons with in situ observations could be helpful to test the proposed method. The method to determine cloud bottoms has the potential to gain more information on PSCs and thin cirrus clouds in the vertical domain. From my point of view, the manuscript is interesting and should be considered for publication in AMT after the following points have been addressed.
Main points:

1. **From my point of view, it seems that the presented PSC classification and the size classification of NAT particles are elaborated separately from the observations. Simulated spectra in Figures 1 and 5 are presented in arbitrary**

units and are scaled individually, while only a few observations are shown separately in Figure 11 using radiance units. Furthermore, only a part of the used spectral range is shown for the observations (it seems that LRS 5 data is not shown). Therefore, the presented plots do not allow to evaluate whether the simulations reproduce details of the observations. From my point of view, this aspect is important, especially if issues related to particle shape are addressed. Overlays or residuals between simulated spectra and observations would allow to evaluate to which degree the underlying assumptions of the classification are supported.

It is correct, our classification method is derived from simulated NAT, STS, and ice PSC spectra. Our intention was to use a wide spread of different situations to stake out the possible range of signals due to variations in the PSC particle size distribution (as done before by Höpfner et al (2006), Spang et al. (2012,2016)). As our detection and classification method is based on relative effects, i.e. colour ratios and brightness temperature differences, we can show where the CRISTA-NF measurements are located in the color ratio and BTD range, without fitting the absolute radiance of each single spectrum. Scaling the spectra to 1 at 833 cm^{-1} (Figs. 1,2,5) helps to point out the relative differences that our method relies on.

We added the second CRISTA-NF channel. We included new figures in the manuscript that show the correlations between the NAT indices/ the BTD and the CI for the observations of CRISTA-NF (Fig. 9) to allow for a comparison with the simulation results (Figs. 3,6). We also included data from additional flights of the RECONCILE campaign to demonstrate that the broad range of simulations covers well the range of observations (Fig. 9).

All results are shown in the new subsection 4.1.

2. **The proposed size classification is based on spectral characteristics of spherical NAT particles. However, field observations (Molleker et al. 2014) and laboratory experiments (Grothe et al., 2006) support a highly aspherical particle shape of large NAT particles or alternative habits. In a well-constrained scenario, the observed spectral fingerprint of large NAT particles has been shown to be clearly better compatible with highly aspherical particles (Woiwode et al., 2016). From my point of view, potential uncertainties of the proposed size classification related to the adopted particle shape should be discussed.**

   The study is based on simulations for spherical particles as this particle shape can be simulated with less computational effort compared to aspherical particles, which is an important factor with respect to the large number of simulations that were carried out. We did not question the existence of aspherical NAT. However, our simulation results demonstrate that spherical particles can produce all the different appearances of the NAT feature (typical feature, shifted feature, step-like behaviour) including those previously attributed to highly aspherical NAT. We think that this is an important point to consider as it implies that IR limb emission measurements alone are not sufficient to derive the existence of aspherical NAT, in particular for cases without additional information on the atmospheric state and cloud particle size distribution.

   Our approach of grouping the NAT particles into 3 size bins based on the spectral signature we do not consider affected by the particle shape for the following reasons. The small particles (< 3 μm) are considered not or only slightly aspherical. In our study we used the term 'small' for particle size distributions with median radii ≤ 1.0 μm. Also Woiwode et al. (2019) use the method by Höpfner et al. (2006), which is based on simulations using spherical particles, to detect these small particles. A substantial fraction of our 'medium' size group (median radii $\leq 4\,\mu$m) can also be considered nearly spherical. The shifted NAT signature reported by Woiwode et al. (2016) for highly ashperical NAT is bi-modal with median radii of 2 and 4.8 μm, where the latter is dominating the signal. This means that the shifted NAT signature that so far was solely attributed to the asphericity, has only been observed in the presence of larger NAT particles. Further, Woiwode et al. (2019, Fig. 1) show that for median radii ≥ 5.0 μm a step-like NAT-feature can be observed. Hence, our result that the shift of the NAT signature is associated with NAT particle size is in line with the results of Woiwode et al. (2016, 2019). Due to particle asphericity our size bin boundary between 'medium' and 'large' has uncertainties. We added these considerations and the contraint that our size bin boundaries are only valid under the assumption of spherical particles to the discussion.

A detailed comparison between the effects of aspherical, mono-modal , and bi-modal spherical cases is beyond the scope of the paper and should be subject of a future study.

3. **The spectral range used by the windows for NAT index-1 to -3 focuses only on the spectral region around the feature at ~820 cm^{-1}. In previous work, it has been shown that, beside details of the spectral feature at ~820 cm^{-1}, the overall spectrum and especially the spectral region towards 960 cm^{-1} respond to particle size and shape (Woiwode et al., 2016). Are there certain (e.g. instrument-related) reasons for not considering the full available spectral range (and particularly the region 960 cm^{-1}) to constrain the size classification and define the criteria?**
   Our detection method is able to detect nearly all simulated NAT scenarios by using the spectral range between 810 and 834 cm^{-1}. It misses only a small part of the very large particles with radii of 8 μm (see Fig. 4 b)). The gradient between 834 cm^{-1} and 950 cm^{-1} is similar for NAT and STS spectra as shown in Fig. 6. We used 950 cm^{-1} instead of 960 cm^{-1} to avoid CRISTA-NF measurement artefacts at the boundary of this channel, but checked in the simulations that both windows deliver similar results. Thus, adding the 950 cm^{-1} spectral region to the classification does not improve the discrimination between NAT and STS.
   Moreover, the simulations for NAT/STS mixtures and bi-modal NAT showed that the region around 950 cm^{-1} is very sensitive to these combinations (see Fig. 5). In our opinion there are multiple ways to obtain similar radiance values in this region. By contrast to this, the spectral feature in the region 810 – 820 cm^{-1} always gives information on the particle type and size, even in the case of the mixtures.

4. **Previous studies showed the spectra of large NAT particles respond significantly to variable radiation from the troposphere/surface, which is scattered by the large particles into the line-of-sight (see Woiwode et al., 2016, 2019). The signal is modulated by the absence or presence of tropospheric clouds. To me it is not clear whether this aspect has been taken into account and which uncertainties might result in the size classification. (Were tropo-**

spheric clouds considered for the discussed flight?
The influence of tropospheric clouds was intensively studied during the analysis of the radiative transfer simulations for various PSC situations for the MIPAS-Env satellite instrument (Spang et al., 2012, 2016) and the results can be transfered to here. A tropospheric cloud below the PSC mainly influences the absolute radiance values where the cold tropospheric cloud leads to lower overall radiance values. The appearance of the spectral signature (typical peak, shifted peak, or step-like behaviour) in the region 810 cm^{-1} to 820 cm^{-1} is nearly unchanged. Simulations by Woiwode et al. (2019) also show this. As our detection method is based on colour ratios, i.e. relative effects, the change of the absolute radiance values does not significantly influence the analysis. Especially in the case of STS or ice, which define the separation lines (see Fig. 3), the data points in the scatter plots only slightly shift along the correlation lines/regions for the specific PSC type. Thus, the separation lines are still valid in such cases.
We added a new subsection 3.2.2 to the manuscript.

5. **Application of the proposed classification scheme is presented for one flight and comparisons with in situ observations are not provided. In situ observations during the same flight suggest particle radii exceeding 7.5 and 10μm (see Molleker et al., 2014,Table 1), while the proposed size classification suggests STS and medium-sized NAT (r=1.5μm – 4.0μm) here. Are these results compatible? A comparison with in situ observations and including further flights could be helpful to evaluate (and potentially optimise) the proposed classification scheme.**
   We applied the proposed classification scheme to all PSC flights (1-5) during RECONCILE. The results are now presented in Figure 9 and discussed in Section 4.1.
   Unfortunatelly, the number of particles with radii $> 7.5\mu$m (59 particles in the whole flight) is the only information about the size distribution during flight 3 (22.01.2010). Without any relation to the number of small particles a serious comment on the agreement between CRISTA-NF and those measurements cannot be made. Grooß et al. (2014) present a size distribution for a part of this flight, which shows that most particle radii lie in the range < about 6 μm with a maximum at about 2.5/3 μm. This agrees with our results. The same is true for flight 4 (shown in Molleker et al. (2014)). However, we refrain from such a simple comparison between in situ observations and our results as there are too many differences between the instruments. Since CRISTA-NF observes all air masses along the line of sight (up to hundreds kilometres away from the aircraft), the air masses detected by the in situ instruments may play only a minor role for the infrared spectra.

6. **Regarding the detection method for cloud bottoms, it would be interesting if the authors could discuss how the method responds if the cloud bottom is located above flight altitude and in the presence of several PSC layers located above each other. Such scenarios are frequently found in polar winters (e.g. Pitts et al., 2018).**
   When the PSC is located above the flight altitude the CI typically increases with decreasing altitude from flight altitude downwards, because the length of the line of sight inside the PSC decreases also. Thus, there is not the typical large increase of the CI indicated by the minimum of the CI gradient when leaving the cloud. Both, the CI

and the CI gradient, typically show the lowest values at the points closest to the flight altitude.

In the case of layered PSCs, where PSCs of different type are lying above each other, the results depend on the optical thickness of the different layers. On the one hand, the CI gradient minimum is still located at the bottom of the complete PSC, when the lower layer is optically thick enough and the transition to the cloud free atmosphere shows the largest increase in CI. On the other hand, when the lower layer is optically very thin, it can occur that the CI gradient minimum is located directly below the upper layer. In this case the transition from the upper layer to the lower layer leads to a larger increase in CI than the transition from the lower layer to the cloud free atmosphere.

We added these information to section 3.5.

Specific comments:

1. **L15, L492 It should be mentioned that the size classification assumes spherical NAT particles.**
   We added the information that the classification is based on spherical particles.

2. **L35 References to further studies focusing on model simulations and comparisons with observations might be considered (e.g. Zhu et al., 2015; Zhu et al., 2017; Khosrawi etal., 2017, Tritscher et al., 2019).**
   We added additional information. See Reviewer 2.

3. **L39ff Further PSC detection techniques (e.g. lidar, in situ) might be mentioned (e.g. Achtert and Tetsche, 2014; Molleker et al., 2014; Pitts et al., 2018).**
   We added information on other measurement techniques.

4. **L51 It should be noted that relatively high volume densities are required for this signature (see Höpfner et al., 2006, 2006b), which are found less frequently in the Arctic.**
   We added this information.

5. **L67, L227 "Very small" should be defined.**
   The sizes that are necessary to shift the spectral feature are evaluated in this paper and the numbers are given later in Sec. 3. Thus, we do not add information in the introduction.
   In the case of the BTD only the particles $< 1.0\ \mu$m lead to a large radiance decrease between the two micro windows. We added this information.

6. **L67 "Another spectral feature" should be explained. To me it seems to be the same spectral signature of beta-NAT particles reported by previous studies, which is modulated by the actual PSC scenario, particle size distribution, particle shape and scattered light from below. "A similar spectral feature" seems more appropriate to me.**
   It is a spectral signature of beta-NAT, but in the first cases it is a peak and here a step-like feature. Thus, it is another appearance of the beta-NAT signature. We corrected this.

7. **L70 It should be mentioned that also other particle modes between 1μm and 6μm were analysed by the same study (see Woiwode et al., 2016, Table 2, Fig. 10ff, Appendix B).**
   We added this information.

8. **L72 It should be mentioned that particle shape and scattered radiation from below where also found to be important parameters by the same study.**
   We added this information.

9. **L127ff Information on the along-track sampling would be helpful.**
   We added this information to Sect. 2.1 as this section describes the CRISTA-NF instrument.

10. **L167 The overall cloud scenario used is well-described. However, the tropospheric cloud scenario and implications for scattered radiation from below, which is scattered by the particles, are not addressed (see 4)).**
    See general comments 4.

11. **L163 Did the simulations account for CFC-12? (spectral band centered at $\sim$920 cm^{-1}).**
    No, because the influence of CFC-12 at 940 cm^{-1} or larger wave numbers is insignificant.

12. **L202, L222 Detailed analysis in the Woiwode et al. (2016) showed that the shape of the feature is sensitive to particle shape.**
    As these sentences only refer to our simulations and explain the observed results, we find that the sentences are correct as they are.

13. **L230ff See 1)-4): The observed spectral fingerprint is not exploited fully to define of criteria of the classification. E.g. the spectral region around 960 cm^{-1}, which was shown to respond significantly to size distributions and particle shape (see Woiwode et al., 2016) is not considered. It is not clear to me whether modulation of the spectra by scattered light from the below is considered. Direct comparisons between observed and simulated spectra are not presented to verify the underlying assumptions.**
    See general comments 1-4.

14. **L279, L314, L336, L507 It should be noted that these statements on the performance are valid within the assumptions made. Verification by direct comparisons of simulated and observed spectra and comparisons with other observations are not provided here.**
    As the whole Section 3 describes our simulations and the derived results, the statements are given with respect to the simulations. Nonetheless, we added some additional information on that.
    In L507 the statement is made with respect to the observations, but as we showed spectra showing the shifted feature and, additionally, added comparisons between simulations and observations (see general comments 1), we think the statement is correct here.

15. **L315ff For comparisons with other studies, it would be helpful to include a Figure showing the used size distributions.**

As the number of scenarios of bi-modal NAT particle size distributions is 115, the number of size distributions is also. We think that this is too much to show all size distributions. Furthermore, all relevant parameters of the size distributions are given in Tab. 3.

16. **L383ff See 6): It would be interesting if the authors could discuss how the method responds if the cloud bottom is located above flight altitude and in the presence of several PSC layers located above each other. Such conditions are frequently found inpolar winters (e.g. Pitts et al., 2018).**
See general comments 6 and section 3.5.

17. **L392 The motivation for choosing the discussed flight should be provided.**
We also included results for other flights (see general comments 1). We show more details for flight 3 as it shows the largest NAT signal of all flights and gives a good example. This information is added.

18. **L397 It would be helpful to indicate the location of the selected two profiles in Fig. 10 and comment on the composition derived in Fig. 10b.**
We added arrows to the Fig 10 a) and b), which are now Fig. 11 b) and c).

19. **L416ff See 5): Considering one case study constitutes only a limited test for a new classification scheme. Further RECONCILE PSC flights, collocated in situ observations and e.g. CALIPSO observations could be used to test (and potentially optimise) the proposed classification scheme.**
We added additional flights (see general comments 1).

20. **L422 Why are only spectra with CI < 3.0 shown here? (compare Fig. 3 and L388)**
The separation between the different types of PSCs and also for the different NAT sizes diminishes with increasing CI. This can be seen in Fig. 4. When all spectra with CI $<$ 5 are considered more of the large particles cannot be detected and also medium size particles are missing. Furthermore, the separation between the different size regimes is not so distinct. Thus it is advisable to use only spectra with CI < 3, as these problems are largely reduced then. We added information to Sect. 3.2.1.

21. **L424 See 1): Figure 11 shows examples of PSC spectra in radiance units, while Figures 1 and 5 show simulations in arbitrary units, which are individually scaled. Clear comparisons between simulations and observations are not possible. Only a part of the used spectral range is shown for the observations (compare L99). Overlays or residuals between simulated and observed spectra using the same units would be helpful to evaluate to which degree the simulations meet details of the observations.**
See general comment 1.

22. **L435,436 See 5): Here, the CRISTA-NF observations are classified as STS or medium sized (median r=1.5-4.0μm) NAT. However, collocated in situ observations suggest particles with radii exceeding 7.5 and 10μm (see Molleker et al., 2014, Table 1). Are these results compatible? It would be interesting to compare size distributions, which are supported by the CRISTA-NF**

simulations, with the in situ observations.
See general comment 5.

23. **L472 The conclusion on the spectral range from 833 to 960 cm^{-1} is not supported sufficiently by Fig. 5, since the spectral range from 840 to 940 cm-1 is not shown.**
In our opinion it is supported. Both spectral ranges are shown and there is no difference between the two spectral ranges in relative as well as in absolute values. Nonetheless, we rephrased the sentence and used the term difference.

24. **L474ff From my point of view, the conclusion "very similar" is not sufficiently supported. The Woiwode et al. (2016,2019) studies used a broader spectral range, higher spectral resolution and spectra in absolute radiance units (which constitutes another "piece of information"). Furthermore, these studies used direct overlays and residuals of simulated observed spectra to analyse the spectral fingerprint of large NAT particles in detail and to define criteria for detection. In the study presented here, the full available spectral range is not exploited and no direct comparisons between simulated and observed spectra are provided. However, within the above mentioned limitations, the conclusion on similarity is supported to some degree by the Woiwode et al. (2016) study, Appendix B, for the small and medium particle sizes. In this study it was shown that for small NAT particles (r=1μm), spherical and aspherical particle populations show an almost identical spectrum, while at r=3μm the signatures start to diverge notably. Furthermore, one might speculate that particles become gradually more aspheric when growing to large sizes, and that (nearly) spherical particles are a suitable assumption at earlier growing stages.**
It is correct that Woiwode et al. (2019) used a wider spectral range, a better resolution etc. for their simulations. Thus, a direct comparison between the two simulations is not advisable. However, as the simulation for the bimodal NAT size distribution shows an enhanced step from 818 to 833 cm^{-1} and no difference between the spectral regions 833 to 960 cm^{-1}, in our opinion the spectrum will fullfil all criteria of the described detection method. For this "comparison" the whole spectrum is not necessary and we simulated all spectral windows used by Woiwode et al. (2019) algorithm. Unfortunately, a direct use of this method is not possible as the absolute radiance values of the two instruments, CRISTA-NF and MIPAS-Envisat, are different (see specific comments 27.).
We rephrased the sentence accordingly.

25. **L476ff It has been shown before that a similar signature can be simulated by assuming spherical particles (see Woiwode et al., 2016, Appendix B). Furthermore it should be noted that the possibility of some variability in the NAT phase regarding particle habits has been clearly mentioned in previous studies (Molleker et al., 2014; Woiwode et al.,2016) and has not been ruled out in the Woiwode et al. (2019) study. However, using the combination of a wide spectral range, high spectral resolution, and supporting information from in situ observations, the Woiwode et al. (2016,2019) studies were not successful in reproducing details of developed spectral fingerprints of large NAT particles by assuming spherical particles. The observed combination of**

a strong “step-like” feature and a flat spectral baseline of the observed spectra towards higher wave numbers (described by the simplified “hockey-stick” picture in Woiwode et al.,2019) could not be reproduced. Close inspection of the spectra showed that Mie simulations of spherical particles always showed significant differences from the observed ”shifted feature” around 820 cm^{-1} and a significant negative slope and/or an “upwardarching” of the spectral baseline at higher wave numbers, and further discrepancies. These discrepancies resulted in significant patterns in the residuals. Using spectral characteristics of highly aspherical particles clearly improved the residuals. Thus, the spectrum clearly includes information on particle shape. Also from other work it is known that infrared spectroscopy allows to infer information on particle shape (Wagner et al., 2005). However, it is understandable to me that within the limited spectral range considered here and without detailed comparisons between observations and simulations a clear decision appears to be not feasible here. From my point of view, the question is not only whether any “hockey-stick” signature can be modelled, but also whether details of the entire accessible spectral fingerprint in developed signatures of large NAT particles can be reproduced, and how the results compare with other observations.

Although our simulations as well as the CRISTA-NF measurements include the three spectral windows, here we consider our 950 cm^{-1} a sufficiently good substitute for the MIPAS 960 cm^{-1} window, proposed by Woiwode et al. (2019) to identify aspherical NAT, we cannot apply the method as it relies on absolute radiances that are inherently different for space-based MIPAS and air-borne CRISTA-NF measurements. However, assuming spherical NAT particles and a bi-modal size distribution our simulated spectra qualitatively reproduce the spectral signature attributed to aspherical particles. To our knowledge Woiwode et al. (2019) did not investigate the effect of bi-modal size distributions on the spectra and hence, we think this should not be ruled out. We rephrased the sentence here.

26. **L477f This sentence should be revisited, since this has been done in before (Woiwode et al., 2016,2019). Of course, any further case studies including in situ comparisons would be helpful to further constrain properties of large NAT particles.**

    Simulations for single spectra are shown, which are in agreement with the FSSPs and the situation. We added a reference. But probably more additional information is necessary as the FSSPs only measure at flight altitude and an infrared limb sounder observes a large volume from flight alitude up to a few hundred kilometres away.

27. **L480f Here, clarification is required. Since absolute radiances are shown in Figure 11, I would expect that integrated radiances and their differences can be calculated.**

    As MIPAS-Envisat is a satellite instrument and CRISTA-NF an airborne instrument and both have significantly different viewing geometries, spectral resolution, spectral sampling, field-of-view, etc., the absolute radiance values are not the same, even when the same air masses have been observed. Thus, also the differences are not the same and the method cannot be applied. We rephrased the sentence for clarification.

28. **L484 See comment to L476ff: it has been shown before that a similar signature can be simulated by assuming spherical particles. However, close inspection showed significant discrepancies between simulated and observed spectra in the case of spherical particles.** Please see answer to comment 25.

29. **Fig 11 The channel LRS 5 seems not to be shown (compare L99).**
We extended the figure and now show also the region around 950 cm^{-1} in the way as for the simulations.

30. **Fig 10 An additional panel including a map with the geolocations of the observations would be helpful to visualize the location and size of the sampled region.**
We added this panel.

Technical corrections

1. **L32 denitrifaction -> denitrification**
corrected

2. **L115 KOPRA should be expanded**
done

3. **L450 CALIPSO and CALIOP should be expanded and a reference should be provided (e.g. Pitts et al., 2018)**
done

4. **L458 transfered -> transferred**
done

5. **L478 FSSP should be expanded and a reference should be provided**
done

6. **L500 GLORIA should be expanded and a reference should be provided**
done

7. **L508 Sentence should be revisited. How can new PSC observations be obtained from the presented method? (Possibly, "observations" should be replaced e.g. by "data set")**
In the preprint version the sentence is: "... new data set of PSC observations ..."

8. **Fig 3, Fig 6 Plots may be refined: data points seem to overlap strongly and it is not clear whether significant populations of data points are hidden below other data points. At least, this should be discussed in the text.**
We added information to the text.

9. **Caption Fig 4 spetrum -> spectrum** done

10. **Fig 7b The x-axis might be scaled from e.g. -4 to >8 for a better focus on the relevant region** We changed the scale to -4 – 8. As the gradient exceeds 20 only at one point we avoid to show the full positive range to show more details in the other range.

2 Comments Reviewer 2

The paper describes methods to detect PSCs and to classify them. The following PSC types are distinguished: NAT (nitric acid trihydtrate), STS (supercooled ternary solution) and ice clouds. For the detection of small NAT particles, a spectral feature at about 820 cm^{-1} has often been used. The authors show, that for larger NAT particles this feature shifts towards smaller wavenumbers and they use this feature to further specify the NAT particles as sNAT (small particles), mNAT (medium particles), and lNAT (large particles). Ice is detected by using the difference between 2 spectral regions (~833 cm^{-1} and ~950 cm^{-1}), the radiance is similar in clear sky conditions but significantly smaller at 950 cm^{-1} when ice is present, a well-known feature which has already been used before. When the cloud is neither NAT nor ice, it is classified as STS. Further a method based on the so-called Cloud Index (CI) is developed to derive the cloud bottom height.
The methods are applied to a comprehensive set of radiative transfer simulations including NAT, ice and STS, all with various concentrations and particle size distributions. Based on the simulations it is demonstrated that the methods work well, in particular sNAT can be distinguished very well from the larger NAT particles mNAT and lNAT. Finally the new methods are also applied to observations of the CRISTA-NF instrument taken during a flight of the RECONCILE campaign
Generally the newly developed methods are described quite well and the figures are appropriate. However, I think that some clarifications are needed, in particular the motivation is not so clear for readers who do not work in the specific field of research (see also my comments below). The scope of the paper fits AMT very well, therefore I recommend publication after taking into account the comments below.
General comments:

1. **The motivation is not clear. It is said in the abstract that there are "uncertainties in the representation of PSCs in model simulations". Which models? Atmospheric chemistry models, climate models? Please provide some examples of models which can be improved by better knowledge of PSC properties. Which properties are required by these models? What are the most relevant parameters? Composition, concentration, size, shape ...? The methods presented here do not derive number concentrations, can these also be derived from spectral IR observations? How important is the classification into different size regimes?**
   Especially, chemistry climate models (CCMs) that are used to asses polar stratospheric ozone loss (e.g. Eyring et al. (2013)) often use rather simple schemes to represent PSCs in the model simulations. Such simplifications may lead to a heterogeneous chemistry dominated by NAT, but it is known that heterogeneous chemistry on STS and cold binary aerosol particles probably dominates the chlorine activation (e.g. Solomon (1999), Drdla and Müller (2012), Kirner et al. (2015)). Additionally, no comprehensive microphysical models are typically used to describe evolution of PSCs over the winter. Mesoscale temperature variations that are known to play an important role for the for-

mation of PSCs (Carslaw et al. (1998), Dörnbrack et al. (2002), Engel et al. (2013), Hoffmann et al. (2017)) are also missing in current state of the art CCMs (Orr et al. (2015)).
Assumptions on the occurence of different PSC types typically have only limited impact on many aspects of ozone loss, as, for example, liquid PSC particles are sufficient to simulate nearly all ozone loss (Wohltmann et al. (2013), Kirner et al. (2015), Solomon et al. (2015)). However, there are also situations where the PSC type is crucial. For example, which PSC type is present at top of ozone loss region is important (Kirner et al. (2015)) and during the initial activation in PSCs covering only a small part of the vortex the type plays also an important role (Wegner et al. (2012)).
Furthermore, the heterogenous reaction rates on PSCs strongly depend on temperature but also on the PSC type (e.g. Drdla and Müller (2012), Wegner et al. (2012)). Here, especially for NAT the reaction rates show rather large uncertainties (Carslaw et al. (1997), Wegner et al. (2012)), which highlights the importance of observing the PSC type.
In summary, information on the compostion of the PSCs is very important, but measurements are limited. Typical PSC measurement techniques are in-situ particle measurements and lidar observations (e.g. Molleker et al. (2014), Achtert and Tesche (2014), Pitts et al. (2018)). But beside these measurement techniques an infrared limb emission sounder builds a good basis for such kind of studies.
We added these information to the introduction.

2. **Cloud optical thickness is a useful parameter to describe a cloud, the term is sometimes used in the paper but no number is given. What is the optical thickness range of the clouds considered here (in the RT simulations and what can be observed using the limb observations)? I suppose that all clouds are optically very thin, what is the upper limit of cloud optical thickness that can be analysed with the presented methods?**
   We added the extinction ranges to Tab. 3 for each individual PSC type. They range from $1.0e^{-5}$ – $1.0e^{-2}$ km^{-1}, whereby the largest extinction is only achieved by ice. For the optical thickness (= extinction * vertical thickness) the range is then $0.5e^{-5}$ to $8.0e^{-2}$ for ice, from $1.05e^{-5}$ to $3.3e^{-2}$ for STS and from $1.7e^{-5}$ to $1.76e^{-2}$ for NAT.
   As the clouds are typically detected using the CI and a threshold value (here 3.0), the upper limit with respect to the optical thickness cannot be stated here. As the CI depends on many different factors (e.g. cloud type, particle radius, altitude of the cloud etc.), the CI values for the same extinction and optical thickness can be different (see General comments Reviwer 3). Thus, the upper limit also depends on these factors influencing the CI and cannot be stated in general.

3. **The radiative transfer simulations are based on a single scattering approach which is not described in detail here. This also means that it is only valid for very thin clouds, for which multiple scattering can be neglected (see e.g. Höpfner and Emde 2005). Please provide the optical thickness range used for the radiative transfer simulations to justify the neglect of multiple scattering.**
   We compared our results with the findings by Höpfner and Emde (2005) and estimated the maximum uncertainties that can occur. In the case of STS the SSA of 0.24 also fits

to our simulations. The scenarios defined in Höpfner and Emde (2005) that fit to our simulations are typically 1 and 2, maybe for a small part of the simulations it is scenario 3. This leads to uncertainties typically $\leq 1\%$ (4.5% for some simulations). In the case of NAT the scenarios are 1 and 2. The SSA lies between the two SSA simulated by Höpfner and Emde (2005) of 0.24 and 0.84. Here we took a mean SSA of 0.54 and a mean uncertainty of the both analysed SSAs. Then for NAT the uncertainty is $\leq 4\%$. For ice the scenarios are mainly 1 and 2 and for a small portion of the simulations (those with the largest volume density) also scenario 3 fits. The SSA is comparable to NAT and we used 0.54. This leads to uncertainties $\leq 4\%$ ($\leq 20\%$ in case of sceanrio 3). In total for almost all simulations the uncertainties are $\leq 4\%$ and only a few simulations have larger uncertainties. But with respect to the computational effort these small uncertainties do not justify the use of multiple scattering.
Furthermore, in our analysis we typically use radiance ratios. As the single scattering approach leads to an underestimation of the radiance that is often similar in many spectral regions, the uncertainties of the ratios are much smaller than the uncertainty of the radiances themselves. E.g. an underestimation of the radiance by 10% in all spectral regions would lead to the same ratios.
We added information to the Sect. 2.2.

4. **Presuambely, the JURASSIC model does not account for horizontal inhomogeneities. Please discuss the validity of this approach for PSCs, i.e. how large is the horizontal extend of the PSCs typically compared to the line of sight through the PSCs?**
Our simulation setup does not account for horizontal inhomogeneities of the PSC. The horizontal extent of the line of sight of the instrument inside the PSC can reach up to several hundred kilometres. In case of synoptic scale PSCs horizontal homogeneity is a good approximation. Other events, such as e.g. mountain wave ice, can lead to PSCs with a smaller horizontal extent. But with respect to the large amount of PSCs simulated in this study we started with the most simple approach regarding the horizontal homogeneity of the PSCs.
We added some information to Sect. 2.2.

5. **For the reader it is rather difficult to remember the definition of all indices used in the paper. I think it would be helpful to include a figure showing the spectral regions used and mark the spectral windows that are used to calculate the individual indices. Also a table including the definitions of NAT-indices 1,2,3 and the CI index could be useful.**
We inserted the different regions into Fig. 1 and numbered the micro windows (MW) from 1 to 7. We additionally added a new table for all indices, where the ratios and BTD that are used can be seen.

6. **I miss some discussion about the uncertainties. For example on p.8 you write: "Nearly all simulations with NAT particles $< 3\mu$m lie above the region of the simulations for STS and ice clouds, which is marked by the solid black line. Thus, NAT particles within this size range can be detected and discriminated using NAT index-1." For the modelled spectra this is correct, but also for real observations? Measurements always include uncertainty, how accurate measurements are required so that NAT is clearly separated**

from the ice clouds?
Because of the strong radiance enhancement caused by the clouds, the dominating uncertainty is the relative uncertainty (noise uncertainty) of the measurements, whereas a systematic uncertainty (e.g. an offset) plays a minor role. The relative uncertainty for the radiances typically observed during atmospheric measurements is about 1–2% for CRISTA-NF (Schröder et al. (2009)). Because of the calculation of ratios, the relative error can add up but is still only a few percent. In the worst case (one MW plus 1-2% and the other MW minus 1-2%) the maximum uncertainty is about 2-4%. For the analysis of the PSC observations this has a different effect depending on the CI and the NAT-index. For smaller values of these quantities the resulting absolute uncertainties of the quantities determined from the relative uncertanties of maximum 4% are smaller than for larger values, e.g. a CI of 2 has a maximum uncertainty of ± 0.08 and a CI of 5 an uncertainty of ± 0.2. Thus, the methods work better for smaller CI values. This suggests to use a threshold value for the CI and to only analyse observations with a CI below this threshold. This suggestion we consider supported by our finding that the separation between the different size bins was better for a CI below 3 (Fig. 3 and Fig. 4). So we keep this value. Furthermore, the same spectral windows are used for CI and NAT index-1/2. In this case some of the uncertainty will cancel, as the data points will shift similar to the correlation regions/lines, i.e. a smaller CI (because of a smaller randiance in the CO_2-window) will be accompanied by a larger NAT index and vice versa. Lastly, the scatter plots for the observations (new Fig. 9), especially for flight 3 and 5, show that a large number of observations exhibit deviations from the separation line larger than a few percent and a clear separation between ice (flight 1) and NAT is visible in Fig. 9 a) and b). Furthermore, the measurements show a compact correlation, which we consider an indications for little noise, whereas we would expect more spread for large noise errors.
Information on the uncertainties are added to the text.

Specific comments:

1. **The title is a bit misleading. The main focus of the paper are the methods to classify and detect PSCs. I thought from reading the title starting with "Radiative transfer" that the paper was more about radiative transfer methods etc. For the RT simulations a well-known model JURASSIC is applied but the methodology is not described in this paper. Also the observational methods are not described here. I think that the title should be something like e.g. "A new method to detect and classify polar stratospheric clouds"**
   We changed the title to:
   A new method to detect and classify polar stratospheric NAT clouds derived from radiative transfer simulations and its first application to airborne IR limb emission observations

2. **Abstract: p1, l7 "... showed a spectral peak at about 816 cm-1 . This peak is shifted compared to the peak at about 820 cm-1, which is known to be caused by small NAT particles. " -> A bit more information about this peak would be helpful. What is the physical process responsible for the peak. Which physical processes could produce a shift of a spectral peak ...**
   The peak at 820^{-1} is mainly caused by emission of radiation. The transformation then

is caused by the increasing contribution of scattering to the total extinction. We briefly added this to the abstract.

3. **p1, l16: "gradient of the CI" -> which gradient is meant here? -> "vertical gradient"**
   yes, we corrected this

4. **p3, l31-33: These 3 sentences should be shifted to Section 2.2**
   These 3 sentences are only a short summary was is comming in the long Sect. 2 in total. The details are then given in the subsections and Sect. 2.2 describes the radiative transfer code JURASSIC. We find that these sentences do not fit to Sect. 2.2. Thus, we stay with the old text.

5. **p4. l19: Title of section should include the term "radiative transfer simulations"**
   we changed the title to "Radiative transfer simulation code JURASSIC"

6. **p4 l32: "The optical properties of the particles, extinction coefficient, scattering coefficient, and phase function, required for the radiative transfer simulations ..." -> "The optical properties of the particles (extinction coefficient, scattering coefficient, and phase function) required for the radiative transfer simulations ...", include brackets here because extinction coefficient, scattering coefficient, and phase function are the optical properties**
   done

7. **p7 l20: What is the "scattering radius" of a particle, this term has not been defined**
   The scattering behaviour of a PSD depends on its median radius μ and distribution width σ and the wavelength. In many cases the effective radius of a PSD is a sufficiently good approximation to describe the scattering behaviour with a single parameter. However, when particle size and wavelength are approximately the same size, this is not a good approximation as the scattering behaviour for two PSDs with same r_{eff} but different μ and σ can be different. Here, the scattering radius r_{sca} is a better single parameter to describe the scattering behavior:

   $$r_{eff} = \frac{\int_{r_0}^{r_1} \pi r^3 n(r) \mathrm{d}r}{\int_{r_0}^{r_1} \pi r^2 n(r) \mathrm{d}r} \tag{1}$$

   $$r_{sca} = \frac{\int_{r_0}^{r_1} \pi r^3 n(r) Q_{sca} \mathrm{d}r}{\int_{r_0}^{r_1} \pi r^2 n(r) Q_{sca} \mathrm{d}r}, \tag{2}$$

   where Q_{sca} is the scattering efficiency depending on radius r, wavelength and complex refractive index e.g. see Hansen & Travis (1974). Since we assumed only one σ in our simulations the PSD median radius is sufficient to unambiguously characterise the scattering behaviour in our study.

   We revised the sentence:
   " The appearance of the spectral feature that is observed in infrared limb spectra in the presence of polar stratospheric clouds consisting of NAT particles in our study is unambiguously characterized by the median radius of the particle size distribution, as we kept the distribution width σ constant."

8. **p7 l31: "different contributions of extinction and scattering" -> extinction is the sum of absorption and scattering, therefore I think that you mean "absorption and scattering"**
   yes, we corrected this

9. **Fig.1 and 5: "spectra have been scaled such that the radiance equals 1" -> scaling factor is not clear, is it the average radiance over the plotted spectral range?**
   The scaling factor is 1/(mean radiance in window 832-834m^{-1}). We added this.

10. **Fig.2: For the interpretation of the RT simulations, it would help to include here also the refractive indices of ice and STS. Further I think that it would be very helpful to show extinction and absorption coefficients, which are probably calculated using Mie theory for the individual PSC types and for some particle sizes to see, that for larger particles the scattering coefficient dominates.**
    We added the refractive indices for STS and ice. Furthermore, we show two more plots now, the extinction and the SSA for NAT with different median radii. These plots illustrate the behaviour of the radiance spectra with increasing median radius. We rephrased the text in Sect. 3.1 accordingly.

11. **p9, l4: "results for PSCs with larger NAT particles (up to 4μm) also lie above the simulations for STS and ice (black separation line)": In Fig.3 it is not well visible, which radii lie above the separation line. May be discrete colours could be used for each of the simulated radii?**
    We used new discrete colours for the Fig. 3. Additionally, we also changed the colours in Fig. 1, Fig. 2, and Fig. 6 to use always the same colours for the NAT, STS, and ice simulations.

12. **p9, l23: "detected NAT spectra" -> NAT is detected, not the "spectra"**
    we rephrased the sentence

13. **p10, l23: "When the NAT detection and classification procedure (described in the previous subsection) is applied to the simulation results for the mixed clouds, the good discrimination between the small and medium size particles remains." -> this is not shown, why?**
    The plot is limited to the range 0.5 to 3.5μm as only a subset of the NAT simulations is combined with STS. Thus, we decided to give the most important numbers regarding the detection capacity in the text and show the plot here in the reply.

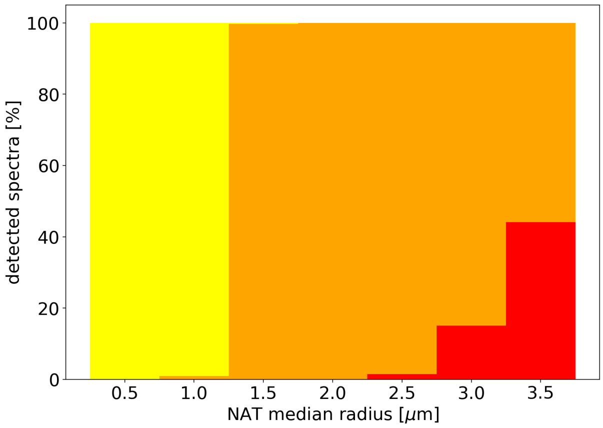

14. **p13, l3-9: Here you discuss about "cloud optical thickness" (thick and thin) without providing any values -> as mentioned above, please quantify the cloud optical thickness**

    The terms thin and thick in this context are relative terms. Unfortunately, a clear relationship between the optical thickness and the CI does not exist (see General comments Reviewer 3). As all different clouds (different type, radius, altiude etc.) enter the analysis here the optical thicknesses can be different for the same CI values.

    Nonetheless, we rephrased the text to clarify the meaning. There are two cases where a bottom altitude cannot be detected. In some cases the observations run into saturation and the CI values below the cloud bottom altitude stay very low. Additionally, in some other situations the CI values below the bottom altitude only show a linear increase and not the larger change directly below the bottom altitude. In both cases the approach fails. A way to sort out such possibly affected observations is the use of a threshold value. For our simulations a CI minimum of 1.25 turned out to be sufficient. Such low values of CI only occur for a part of the ice clouds simulated here (typically that with the largest volume densities and for a few of the NAT and STS clouds with large HNO_3 VMRs ($\geq$ 11 ppbv) or volume densities ($\geq 5\ \mu\ m^3/cm^3$) combined with a large vertical thickness ($\geq$ 4 km).

15. **p15, l7: "... where much more NAT was observed by CALIOP (the difference in the Southern hemisphere is much smaller)"-> how much more NAT was observed by CALIOP, how much smaller is the difference in the Southern hemisphere?**

    The agreement for NAT in the Southern hemisphere is 73%, whereas there is only an agreement of 18% in Northern hemisphere. We added these numbers to the text.

16. **p16 l20: "This method can surely be transferred to other cloud observations such as cirrus clouds and aerosol layers and to other airborne instruments measuring in the same wavelength region like e.g. GLORIA." -> Which clouds and aerosols could be observed? Probably only very thin clouds? Up to which cloud optical thickness can the method be applied?**

    As said before, our method rely on the CI and there is no clear relationship between the CI and the optical thickness (see General comments Reviewer 3). Thus, a clear statement cannot be made as the upper limit depends on many factors.

3 Comments Reviewer 3

This paper demonstrates the clear capability of infrared FTS limb sounders to provide detection, discrimination of particle types and particle sizing in polar stratospheric clouds and is an advance on the current state of the art. The paper is acceptable for publication following some minor corrections.
General comments:

1. **I strongly suggest that an attempt is made to make an additional plot that shows the optical depth vs CI for some samples of different PSC cloud types. Likewise the CI vertical gradient is related to the optical thickness gradient.**
   Unfortunately, there is no clear relationship between the optical depth and the CI. Different parameters can influence the CI that leads to different values although the optical depth is the same.
   Spang et al. (2008) already showed that the CI depends on the altitude and that additionally the background atmosphere (e.g. polar winter vs. tropics) can have a large influence. Griessbach et al. (2014) showed that the observed radiance, and thus the CI, also depends on the radius of the particles. In Griessbach et al. (2020) the authors showed that there is some correlation between CI and extinction for ice and volcanic aerosol but a distinct relationship could not be determined. CIs of large particles (r > 5 μm) are more related / show a quite good correlation with the integrated surface area densities along the line of sight or for ice with the ice water path divided by effective radius (Spang et al. (2012, 2015)). We also did some studies with the new simulations and found similar results. Furthermore, the particle type also plays a role as the spectral slope of the extinction is different for the different particle types. Thus, the radiance enhancement in the regions used for the CI can be different although the total extinction and thus the optical depth are the same. As a consequence the CI values can only be related to an optical depth when all influencing parameters (altitude and thickness of cloud, particle type and radius, background atmosphere) are known, which is typically not the case. Therefore, we cannot give numbers in this direction in the paper as there are too many unknowns.

Specific comments and typos

1. **Page 2 L35: "incomplete" rather than "difficult"?**
   changed the term

2. **L37-38: [An] infrared .... build[s]...**
   done

3. **L39: sounder[s]**
   done

4. **L44-45: make distinction between CO2 molecular line emssion and broader continuum like aerosol emission?**
   we rephrased the sentence

5. **L51: color => colour**
   done

6. **Page 3 L64-65: Maybe make clearer that for an airborne instrument the limb tangent moves away from the aircraft for downward looking views.**
   we added information

7. **L72: What about changes with the aspect ration of the particles?**
   We added information that it also depends on shape and radiation scattered from below. See Reviewer 1.

8. **L86: itselves => themselves**
   done

9. **Page 4 L87: JURASSIC is not defined until L106**
   we added the definition

10. **L110: PREMIER IRLS is not defined**
    we added the definition

11. **L111: spectral/ly/**
    done

12. **L115: KOPRA is not defined**
    done

13. **Page 5 L130: What about spectral regions for STS and background binary sulfate aerosols?**
    As STS and the background binary sulfate aerosol have no distinct spectral features like a peak nor a clear slope of the extinction such as ice, there are no special regions for STS and the background aerosol.

14. **L133: al[t]itude**
    done

15. **L139: reference to a rejected ACPD paper?**
    The paper has not been rejected, but the reply to the reviewer comments and the upload of a revised manuscript have not been done. However, it is the best paper describing the atmosphere and it has been cited far more than 100 times.

16. **Page 6 L177: median radius varied in steps of?**
    For small particles it has been varied in steps of 0.5 μm, then in steps of 1 μm, and at the end there is one step of 2 μm. Because of the different step sizes all used radii are summarised in Tab. 3.

17. **Page 8 L215: imaginary part/s/**
    done

18. **L234-249 and everywhere else including figure captions and tables: Is it possible to give all these spectral regions a distinct short name? e.g. R1, R2, R3 etc Otherwise the reader has to scan the characters and check to see which regions are the same thing rather than seeing that immediately from the short name.**
    We added a table for all indices and we marked the regions in Fig. 1 (see Reviewer 2).

Additionally, we numbered the micro windows (MW) from 1 to 7 and added the short names like MW1 at the corresponding text positions.

19. **Page 9 L257: an[d]**
    done
20. **Page 10 L312: less => fewer**
    done
21. **Page 11 L335: mille => thousand**
    done
22. **Page 13 L408: extend => extent**
    done
23. **Page 15 L463: called [a] hockey-stick**
    done
24. **Page 16 L494: What are the detection levels of the new method compared to the old method? e.g. in terms of the minimum volume density um3/cm3.**
    The detection level for the small particles is the same as for the old method, as they are detected with the same method. The improvement of our method is that the detection is expanded to larger NAT particle sizes that are not detectable with the old method.
25. **L501: "minimisation" means "reduction"?**
    yes, we changed this
26. **L507: "safely" means "always"?**
    we removed safely
27. **Figures 3, 6 and 7: Can an approximate optical depth scale be put on the x-axis?**
    Unfortunately, there is no distinctive relationship between optical depth and CI (see General comments).
28. **Figure 8: What are the actual optical depths corresponding to these CI values?**
    Unfortunately, there is no clear relationship between optical depth and CI (see General comments). As clouds with many different parameters enter this plot, the answer cannot be given.

A new method to detect and classify polar stratospheric NAT clouds derived from radiative transfer simulations and its first application to airborne IR limb emission observations

Christoph Kalicinsky[1], Sabine Griessbach[2], and Reinhold Spang[3]

[1]Institute for Atmospheric and Environmental Research, University of Wuppertal, Germany
[2]Forschungszentrum Jülich, Jülich Supercomputing Centre, JSC, Jülich, Germany
[3]Forschungszentrum Jülich, Institut für Energie und Klimaforschung, Stratosphäre, IEK-7, Jülich, Germany

Correspondence: C. Kalicinsky (kalicins@uni-wuppertal.de)

Abstract. Polar stratospheric clouds (PSCs) play an important role for the spatial and temporal evolution of trace gases inside the polar vortex due to different processes, such as chlorine activation and NOy redistribution. As there are still uncertainties in the representation of PSCs in model simulations, detailed observations of PSCs and information on their type ~~(~~ , nitric acid trihydrate (NAT), supercooled ternary solution (STS), and ice~~)~~ , are desirable.
The measurements inside PSCs by the airborne infrared limb sounder CRISTA-NF (CRyogenic Infrared Spectrometers and Telescope for the Atmosphere – New Frontiers) during the RECONCILE (Reconciliation of essential process parameters for an enhanced predictability of Arctic stratospheric ozone loss and its climate interactions) aircraft campaign showed a spectral peak at about 816 $\mathrm{cm^{-1}}$. This peak is shifted compared to the known peak at about 820 $\mathrm{cm^{-1}}$, which is known to be caused by emission of radiation by small NAT particles. To investigate the reason for this spectral difference we performed a large set of radiative transfer simulations of infrared limb emission spectra in the presence of various PSCs (NAT, STS, ice, and mixtures) for the airborne viewing geometry of CRISTA-NF. NAT particles can cause different spectral features in the region 810 – 820 $\mathrm{cm^{-1}}$. The simulation results show that the appearance of the feature changes with increasing median radius of the NAT particle size distribution from a peak at 820 $\mathrm{cm^{-1}}$ to a shifted peak and, finally, to a step-like feature in the spectrum, caused by the increasing contribution of scattering to the total extinction.. Based on ~~this behaviour~~ on the appearance of the spectral feature we defined different colour indices to detect PSCs containing NAT particles and to subgroup them into three size regimes: small NAT ($\leq$ 1.0 µm), medium NAT (1.5 – 4.0 µm), and large NAT ($\geq$ 3.5 µm) under the assumption of spherical particles. Furthermore, we developed a method to detect the bottom altitude of a cloud by using the cloud index (CI), a colour ratio indicating the optical thickness, and the vertical gradient of the CI. Finally, we applied the methods to observations of the CRISTA-NF instrument during one local flight of the RECONCILE aircraft campaign and found STS and medium sized NAT.

1 Introduction

Polar stratospheric clouds (PSCs) form inside the cold polar vortices in both hemispheres in winter. They have a major influence on the ozone chemistry and thus the ozone depletion in the stratosphere (Solomon, 1999). PSCs are classified into three different types: supercooled ternary solution (STS) droplets, nitric acid trihydrate (NAT), and ice particles (e.g. Lowe and MacKenzie, 2008). The formation and existence of these different types is largely temperature dependent. Solid ice particles can only exist below the frost point $T_{\mathrm{frost}} \approx 188\ \mathrm{K}$, whereas NAT particles are thermodynamically stable at temperatures below $T_{\mathrm{NAT}} \approx 195\ \mathrm{K}$. The liquid STS droplets form from binary H_2SO_4-H_2O droplets at temperatures below the dew point of HNO_3 $T_{\mathrm{dew}} \approx 192\ \mathrm{K}$ by the uptake of HNO_3 (see e.g. Peter and Grooß, 2012, and references therein).

PSCs directly and indirectly influence the spatial distribution of trace gases relevant for ozone depletion in different ways. Due to heterogenous reactions on the cold particle surfaces chlorine is activated from its reservoir species, mainly HCl and $ClONO_2$, and the chlorine radicals catalytically destroy ozone (e.g. Solomon, 1999). NAT particles can grow to larger sizes, which then leads to a sedimentation of the particles and thus to a permanent removal of HNO_3 from the stratosphere (denitrification) (e.g. Fahey et al., 2001; Molleker et al., 2014). This denitrification slows down the deactivation of chlorine and thus enhances the ozone loss (e.g. Waibel et al., 1999; Peter and Grooß, 2012).

Because of these different processes and due to the fact that many models rely on rather simple parametrisations, the simulation of PSCs and related processes is ~~difficult~~ incomplete and partly accompanied with larger uncertainties. ~~(see Spang et al., (2016,2018) for more detailed discussions). Thus, as many observations of PSCs as possible and a detailed discrimination into the different particle types are necessary to enhance the understanding of the relevant processes and reduce the uncertainties.~~ Especially, chemistry climate models (CCMs) that are used to asses polar stratospheric ozone loss (e.g Eyring et al., 2013) often use rather simple schemes to represent PSCs in the model simulations. Such simplifications may lead to a heterogeneous chemistry dominated by NAT, but it is known that heterogeneous chemistry on STS and cold binary aerosol particles probably dominates the chlorine activation (e.g Solomon, 1999; Drdla and Müller, 2012; Kirner at al., 2015). Additionally, no comprehensive microphysical models are typically used to describe evolution of PSCs over the winter. Mesoscale temperature variations that are known to play an important role for the formation of PSCs (Carslaw et al., 1998; Dörnbrack et al., 2002; Engel et al., 2013; Hoffmann et al., 2017) are also missing in current state of the art CCMs (Orr et al., 2015).

Assumptions on the occurence of different PSC types typically have only limited impact on many aspects of ozone loss, as, for example, liquid PSC particles are sufficient to simulate nearly all ozone loss (Wohltmann et al., 2013; Kirner at al., 2015; Solomon et al., 2015). However, there are also situations where the PSC type is crucial. For example, which PSC type is present at top of ozone loss region is important (Kirner at al., 2015) and during the initial activation in PSCs covering only a small part of the vortex the type plays also an important role (Wegner et al., 2012). Furthermore, the heterogenous reaction rates on PSCs strongly depend on temperature but also on the PSC type (e.g. Drdla and Müller, 2012; Wegner et al., 2012). Here, especially for NAT the reaction rates show rather large uncertainties (Carslaw et al., 1997; Wegner et al., 2012), which highlights the importance of observing the PSC type.

In summary, information on the compostion of the PSCs is very important, but measurements are limited. Typical PSC measurement techniques are in-situ particle measurements and lidar observations (e.g. Molleker et al., 2014; Achtert and Tesche, 2014; Pitts et al., 2018). But beside these measurement techniques an infrared limb emission sounder builds a good basis for such kind of studies (e.g. Spang and Remedios, 2003; Höpfner et al., 2006).

Besides the derivation of volume mixing ratios of several trace gases, infrared limb emission sounders such as CRISTA (CRyogenic Infrared Spectrometers and Telescopes for the Atmosphere; Offermann et al., 1999; Grossmann et al., 2002), CRISTA-NF (CRyogenic Infrared Spectrometers and Telescope for the Atmosphere – New Frontiers; Kullmann et al., 2004), and MIPAS-Envisat (Michelson Interferometer for Passive Atmospheric Sounding - Envisat; Fischer et al., 2008) are well suited to detect clouds of different composition. Spang et al. (2001) established a simple and effective way for cloud detection based on the radiance ratio of two specific spectral regions. The first one is dominated by CO_2 molecular line emissions (around 792 cm^{-1}) and the second one by the broader continuum like aerosol emissions ~~of aerosol~~ (around 833 cm^{-1}). This detection method was then succesfully used in various studies and for different satellite and airborne instruments (e.g. Spang and Remedios, 2003; Spang et al., 2002, 2005, 2008, 2015; Höpfner et al., 2006; Kalicinsky et al., 2013). Furthermore, the infrared spectra exhibit different spectral features or radiance behaviours in the presence of polar stratospheric clouds of different type. Spang and Remedios (2003) presented a sharp peak-like feature at around 820 cm^{-1} observed by the CRISTA instrument in the Antarctic winter for the first time. They attributed this feature to HNO_3-containing particles. Höpfner et al. (2006) showed that the feature can be best reproduced in simulations by using refractive index data for β-NAT particles (assuming relatively high number densities). The authors showed that the colour ratio method derived by Spang and Remedios (2003) that exploits the peak-like feature for detection is able to identify PSCs containing small NAT particles (radii < 3 µm). By means of a large set of radiative transfer simulations Spang et al. (2012, 2016) developed a detection and discrimination method for PSCs. Besides the feature at 820 cm^{-1}, the method also uses further spectral behaviours such as a radiance decrease from around 830 cm^{-1} towards larger wavenumbers (around 950 cm^{-1}) that occurs in the case of ice to distinguish different PSC types. Spang et al. (2018) finally presented a climatology of the PSC composition for the whole MIPAS-Envisat observation time period (2002 – 2012) based on this method.

During the RECONCILE campaign (Reconciliation of essential process parameters for an enhanced predictability of Arctic stratospheric ozone loss and its climate interactions; von Hobe et al., 2013) a slightly different type of spectral feature was observed by the infrared limb emission sounder CRISTA-NF in the presence of PSCs. The campaign took place in Kiruna, Sweden, in January to March 2010 and the high-flying research aircraft M55-Geophysica carried out a number of flights with a huge set of different instruments to study the polar vortex and related scientific topics such as PSCs, ozone chemistry, or mixing processes. CRISTA-NF was one of the operated instruments and the instrument is able to detect clouds and distinguish different types of PSCs. During the first five flights of the campaign (17.01. – 25.01.2010) CRISTA-NF detected PSCs around the aircraft. Because of the viewing geometry of an infrared limb sounder, where the tangent points move away from the aircraft with decreasing samping altitude, CRISTA-NF typically observes air masses in a wider range around the aircraft. The infrared spectra measured inside the clouds show a noticeable spectral feature at about 816 cm^{-1}. This feature is slightly shifted towards smaller wavenumbers compared to the typical spectral feature at 820 cm^{-1}, which is caused by very small NAT particles. Another appearance of the spectral feature caused by NAT particles, a step-like or shoulder-like behaviour of the radiance in the spectral region 810 – 820 cm^{-1}, has been observed by the ballon-borne instrument MIPAS-B in January 2001 (Höpfner et al., 2002) and the airborne instrument MIPAS-STR during the ESSENCE campaign in December 2011 (Woiwode et al., 2016). Woiwode et al. (2016) analysed different particle modes with radii between 1 and 6 µm and suggested that highly aspherical medium/large sized (median radius 4.8 µm) NAT particles caus~~ing~~ed the change of the NAT signature to the step-like appearance. Woiwode et al. (2016) concluded that the particle shape and the scattered radiation from below can influence the feature. However, ~~Thus,~~ the appearance of the spectral feature seems to depend on the particle size distributions of the NAT particles, especially on the median radius. This motivated the following study of the relationship between the appearance of the feature (typical, shifted, and step-like) and the corresponding particle size distribution aiming at an improved detection method for PSCs containing NAT particles. Especially the possibility to detect larger NAT particles is important, because they play the major role for the denitrification of the stratosphere (Fahey et al., 2001; Molleker et al., 2014), and thus for the whole ozone chemistry (e.g. Waibel et al., 1999; Peter and Grooß, 2012). New insights and an improvement of the detection method is also interesting for measurements of other infrared limb emission sounder such as MIPAS-Envisat, where data for a long observation period (about 10 years) and both hemispheres are available. For this purpose a large variety of different PSCs with respect to the composition, spatial dimensions, and particle size distributions of the PSC particles was simulated and analysed. The paper is structured as follows. In Sect. 2 the CRISTA-NF instrument and the radiative transfer code are described and the setup used for the simulations is explained. The results of the simulations are presented and analysed in Sect. 3. The derived methods are applied to the CRISTA-NF measurements in Sect. 4. Finally, the main results are summarised in Sect. 6.

2 Methods and setup

The radiative transfer simulations were performed using the viewing geometry and spectral properties of the airborne infrared limb sounder CRISTA-NF. The background atmosphere used for the simulations is a polar winter atmosphere with conditions suitable for the formation of polar stratospheric clouds. The simulations ~~it~~themselves were performed using the ~~radiative transfer code~~ Juelich Rapid Spectral Simulation Code (JURASSIC). This section describes the CRISTA-NF instrument, the JURASSIC radiative transfer code, the setup used for the simulations, and the different cloud scenarios that were investigated.

2.1 CRISTA-NF istrument

The airborne CRISTA-NF instrument is a successor of the satellite instrument CRISTA. CRISTA-NF measures the thermal emissions of the atmosphere in the mid-infrared region from 4 to 15 µm in an altitude range from flight altitude (up to 20 km) down to approximately 5 km. A detailed description of the design of the cryostat and the optical system is given by Kullmann et al. (2004). The calibration procedure and some improvements for the RECONCILE campaign are described by Schroeder et al. (2009) and Ungermann et al. (2012), respectively.

CRISTA-NF uses a Herschel telescope and a tiltable mirror to scan the atmosphere from flight altitude down to approximately 5 km. The incoming radiance is then spectrally dispersed by two Ebert-Fastie grating spectrometers (e.g., Fastie, 1991). These two spectrometers have different spectral resolving powers of $\frac{\lambda}{\Delta\lambda} \approx 1000$ and 500, respectively, and are therefore denoted as high resolution spectrometer (HRS) and low resolution spectrometer (LRS). In this study we focus on the spectral range that is covered by the two channels LRS 5 (850 – 965 cm^{-1}) and LRS 6 (775 – 865 cm^{-1}). The vertical sampling of the LRS during one altitude scan is typically between 100 and 200 m with finer sampling at higher altitudes and a wider one at lower altitudes due to mounting and instrument conditions. The field of view (FOV) is very small with 3 arcmin (about 300 m at 10 km tangent height; Spang et al., 2008). The horizontal sampling along the flight track is about 12.5 to 15 km depending on the speed of the aircraft. The radiance is finally measured using liquid helium cooled semiconductor detectors (Si:Ga) that are operated at a temperature of 13 K. These low temperatures enable fast measurements of one spectrum in about one second.

2.2 Radiative transfer simulation code JURASSIC

For the simulations of the CRISTA-NF infrared spectra in the presence of PSCs we used the Juelich Rapid Spectral Simulation Code (JURASSIC) (Hoffmann, 2006). It is a fast radiative transfer model for the mid-infrared spectral region. It was used in numerous studies analysing infrared limb and nadir measurements, including MIPAS-Envisat (Hoffmann et al., 2005, 2008), CRISTA-NF (Hoffmann et al., 2009; Weigel et al., 2009), and the nadir sounder AIRS (Hoffmann and Alexander, 2009), and to simulate 2-D trace gas and temperature retrievals for a proposed new infrared limb instrument named PREMIER IRLS (PRocess Exploitation through Measurements of Infrared and millimetre-wave Emitted Radiation – InfraRed Limb Sounder; Preusse et al., 2009; Hoffmann and Riese, 2010). For fast radiative transfer calculations, JURASSIC applies a spectral~~ly~~ averaging approach by using the emissivity growth approximation (EGA) (Gordley and Russel III, 1981; Marshall et al., 1994) and precalculated look-up tables. The look-up tables were calculated by the line-by-line model reference forward model (RFM; Dudhia, 2017) and take into account the spectral resolution of the instrument to be investigated.
JURASSIC has been compared to the line-by-line models RFM and KOPRA (Karlsruhe Optimized and Precise Radiative transfer Algorithm) for selected spectral windows and shows good agreement (Griessbach et al., 2013). JURASSIC was extended with a scattering module that allows for radiative transfer simulations including single scattering on aerosol and cloud particles (Griessbach et al., 2013). The optical properties of the particles (extinction coefficient, scattering coefficient, and phase function) required for the radiative transfer simulations with scattering, can either be calculated with an internal Mie code assuming spherical particles, or can be taken from databases for non-spherical particles. The scattering module was successfully used in different studies (Griessbach et al., 2014, 2016, 2020).

2.3 Simulation setup

The simulation setup can be divided into three parts: the instrument part, the atmosphere part, and the cloud scenarios. The instrument part includes the viewing geometry and the spectral properties of the airborne infrared limb emission sounder CRISTA-NF. In the atmosphere part we describe the background atmosphere that is used for the simulations. All different types of polar stratospheric clouds with respect to the position and thickness of the cloud as well as the composition (NAT, STS, ice) are summarised in the cloud scenario section.

2.3.1 Instrument properties

The two important spectral regions that are necessary to analyse infrared spectra with respect to polar stratospheric clouds are 785 – 840 cm^{-1}, because of the cloud index (CI) and the NAT signature, and the region 940 – 965 cm^{-1}, because of an ice signature. The spectral resolving power used in the simulations is $\frac{\lambda}{\Delta\lambda}$ = 536 at a reference wavelength of 12.5 $\mu\mathrm{m}$ (800 cm^{-1}) (see Weigel, 2009). The spectral sampling of the CRISTA-NF measurements is about 0.0065 $\mu\mathrm{m}$ that corresponds to an average of 0.42 cm^{-1} for the wavelength range 785 – 840 cm^{-1} and 0.59 cm^{-1} for the region 940 – 965 cm^{-1}. These values have been considered in the calculation of the look-up tables for JURASSIC. We used an observer altitude of 18.4 km, which is the maximum average flight altitude during the RECONCILE flights of interest. However, the average altitudes of all flights only differ by a few hundred meters (18.1 to 18.4 km). The observations were simulated in the altitude range from observer altitude down to 10 km. The vertical sampling used for the simulations was 100 m. Tab. 1 summarises these properties.

2.3.2 Atmospheric setup

For the background atmosphere we used polar winter conditions to get representative simulations. Most information are taken from the MIPAS reference polar winter climatology by Remedios et al. (2007). For some constituents we made updates and here we focused on the winter 2009/2010, especially on the January 2010. There are two reasons for this choice: 1. A large variety of PSCs has been observed in the Arctic in this winter. 2. The CRISTA-NF observations of PSCs during RECONCILE took place in January 2010. The updates are summarised in the following part.

Two very important parameters of the atmosphere for the simulation of infrared spectra are temperature and CO_2 volume mixing ratios (VMR). In order to have a temperature profile that is representative for a situation where many different PSCs can occur we focused on the observation period of PSCs during the RECONCILE aircraft campaign (17 to 25 January 2010). The temperature profile was derived using ERA-Interim reanalysis data (Dee et al., 2011). An average profile in the region of the CRISTA-NF observations north of Kiruna (67° – 78° N, 10° – 35° E) was used for the background atmosphere. Additonally, we used the corresponding pressure profile from ERA-Interim reanalysis data. The CO_2 VMR we derived from the reconstructed CO_2 product by Diallo et al. (2017) for January 2010. The profile is a zonal average in the latitude region of interest. The profiles were extended to larger altitudes following the slope of the climatology. As PAN (peroxyacetyl nitrate) is not included in the climatology, we took a mean profile derived from CRISTA-NF observations (see Ungermann et al. (2012) for retrieval description) in the region around Kiruna between end of January and begin of March. Unfortunately, there are no retrieval results for PAN during the PSCs flights available. However, the derived profile is in a good agreement with published MIPAS-Envisat observations for October to December 2003 in the corresponding latitude region (Glatthor et al., 2007) and also with the average profile in 2007/08 in the latitudinal band 60° – 90° (Pope et al., 2016). For CFC-11, CFC-113, HCFC-22, SF_6, and COF_2 we updated the climatological profiles to 2010 values by using information of tropospheric values (Bullister, 2011) as well as satellite observations by ACE-FTS (Boone et al., 2013) and in-situ observations carried out by the HAGAR instrument (Riediger et al., 2000; Werner et al., 2010) onboard the M55-Geophysica during RECONCILE.

In order to save computation time we restricted the number of trace gases to a minimum by just using those gases that have a noticeable contribution to the total radiance in the two analysed spectral regions. The trace gases have been selected seperately for the two spectral regions. For the region 785–840 cm^{-1} we used 13 trace gases: CO_2, HNO_3, $ClONO_2$, O_3, H_2O, HNO_4, CCl_4, CFC-11, HCFC-22, CFC-113, PAN, ClO, NO_2. The simulations in the region 940–965 cm^{-1} included 9 trace gases: CO_2, HNO_3, O_3, H_2O, CFC-11, PAN, SF_6, NH_3, COF_2. A summary of the trace gases, their sources, and the spectral region in which they ~~have been~~ were considered is given in Tab. 2.

2.4 Cloud scenarios

Two parameters that were largely varied to investigate different situations are the position and the thickness of the PSCs. The PSC position was varied between a minimum cloud bottom height (CBH) of 13 km and a maximum top height of 30 km. ~~In the case of~~ For the thickness we used the values 0.5, 1.0, 2.0, 4.0, and 8.0 km. The bottom height is shifted in 1 km steps up to 20 km (slightly above flight altitude) and in 2 km steps above for each thickness value as long as the cloud top height (CTH) is lower or equal to 30 km.

PSCs consisting of NAT particles are the most interesting ones for this study, because of their impact on the NOy redistribution. Thus, the largest part of the simulations were performed for this particle type. The two parameters varied for the NAT scenarios are the median radius of the particle size distribution and the number density of the particles. The different particle size distributions for all cases (also ice, STS) were described by a log-normal distribution

$$\frac{\mathrm{d}N}{\mathrm{d}r} = \frac{N_0}{\sqrt{2\pi}\ln(\sigma)r} e^{-\frac{(\ln(r)-\ln(\mu))^2}{2\ln^2(\sigma)}}, \qquad (1)$$

where r is the radius, N_0 is the number density, μ is the median radius, and σ is the width. The width is constant at $\sigma = 1.35$ and we varied the median radius between 0.5 and 8.0 µm. For the calculation of the number densities and thus the particle size distributions we used different HNO_3 VMRs from 1 to 15 ppbv under the assumption that one HNO_3 molecule is converted to one NAT molecule. The calculations were done for typical conditions for the lower stratosphere with 193 K and 60 hPa.

~~Furthermore,~~ We also simulated PSCs using bimodal NAT particle distributions. The median radius of the first mode varied from 0.5 to 2.5 µm and was combined with a second mode, where larger radii than in the first mode were used. The total HNO_3 VMR was always 10 ppbv and the ratios between first and second mode were 70/30, 50/50, and 30/70. Here, we ~~only simulated~~ restricted the simulations to two bottom altitudes at 13 and 17 km and three different thicknesses 1, 4, and 8 km.

~~Additonally, we performed simulations for the PSC particle types STS and ice.~~ The volume densities used for ~~these~~ the STS and ice simulations range from 0.1 – 10.0 $\mu m^3/cm^3$ and from 0.1 – 100.0 $\mu m^3/cm^3$ ~~for STS and ice~~, respectively. The median radii were varied between 0.1 and 1.0 µm for STS and between 1.0 and 10.0 µm for ice. In the case of STS we simulated three different mixtures of H_2SO_4/HNO_3 with wt% of 2/48, 25/25 and 48/2.

Finally, we simulated mixed NAT/STS clouds. Here, we also used only the bottom altitudes at 13 and 17 km and the different thicknesses 1, 4, and 8 km like in the case of bimodal NAT. Furthermore, we concentrated on the small and medium size NAT particles up to 3.5 µm and used three different HNO_3 VMRs of 5, 10, and 15 ppbv. We combined these NAT scenarios with STS scenarios using wt% 2/48, volume densities of 5 and 10 $\mu m^3/cm^3$, and radii of 0.1, 0.3, and 1.0 µm.

The parameter ranges for all cloud scenarios are summarised in Tab. 3 including the cloud extinction range. The refractive indices for ice, NAT, and the STS mixtures were taken from Toon et al. (1994), Biermann (1998) with refinement in Höpfner et al. (2006), and Biermann et al. (2000), respectively. The total number of scenarios was 16392 (NAT: 9240, STS: 3360, ice: 2352, and mixtures bimodal NAT and NAT/STS: 1440).

Considering the computational resources required to simulate this amount of scenarios we assumed single scattering. Neglecting multiple scattering introduces uncertainties. Based on the findings of Höpfner and Emde (2005) for our optical depth ranges (Tab. 3, extinction times cloud thickness) and the single scattering albedos of STS, NAT and ICE the uncertainty is mostly below 1%, 4%, and 4%, respectively. Only for a few scenarios of 8km thickness the uncertainty may reach up to 4.5% for STS and 20% for ice. In the cloud scenario setup we assumed homogeneous clouds. The horizontal extent of the CRISTA-NF line of sight inside the PSC can reach up to several hundred kilometres. In case of synoptic scale PSCs horizontal homogeneity is a sufficiently good approximation. PSCs of other origin, e.g. mountain wave induced PSCs, have a smaller horizontal extent, but are less frequent compared to synoptic scale PSCs.

3 Results of the simulations

The following section deals with the analyses of the simulation results. The analyses can be divided into three parts. 1. The shift of the NAT feature; 2. The detection of PSCs and the identification of the PSC types NAT and ice; 3. The determination of the bottom altitude of the clouds.

3.1 Shift of the NAT feature

The appearance of the spectral feature that is observed in infrared limb spectra in the presence of polar stratospheric clouds consisting of NAT particles ~~depends on the median radius of the particle size distribution (more accurate it depends on the scattering radius, which itself depends on the median radius and the width σ).~~ in our study is unambiguously characterized by the median radius of the particle size distribution, as we kept the distribution width σ constant With increasing median radius the shape transforms from the well known pronounced peak at about 820 cm^{-1} to a peak, which is slightly shifted towards smaller wavenumbers, and, finally, to a step-like feature. Figure 1 illustrates this behaviour and the dependency of the appearance on the median radius. The spectra shown in Fig. 1 ~~have been~~ are scaled such that the radiance in the spectral range 832.0 – 834.0 cm^{-1} is equal to one for all spectra. The example spectrum for the smallest median radius of 0.5 µm (yellow colour) exhibits a clear pronounced peak at about 820 cm^{-1}. For slightly larger median radii (1.0 – 3.5 µm) the peak shifts to smaller wavenumbers and becomes less pronounced (orange colours). When the median radius is even larger the spectral feature transforms to a step-like feature that shows a steep radiance decrease from about 811 cm^{-1} to 826 cm^{-1}. The magnitude of this decrease largely diminishes with increasing median radius.

This behaviour and thus the dependency of the appearance of the feature on the median radius can be explained by the different contributions of ~~extinction~~ emission/absorption and scattering to the total observed radiance enhancement caused by the PSCs. These contributions largely depend on the median radius of the particles. The real and the imaginary part of the refractive index of β-NAT are shown in Fig. 2 a) in black and red, respectively. The imaginary part~~s~~ illustrates the emission and absorption characteristic of the NAT particles whereas the real part shows the scattering behaviour. The imaginary part shows a distinct peak at about 820 cm^{-1}. As the emission is the major contribution when only small particles are present the simulated spectra in case of small NAT only show this peak. This is illustrated in Fig. 2 b) and c), where the extinction and single scattering albedo (SSA) are shown. The extinction shows a clear peak at about 820 cm^{-1} and the SSA, which gives the contribution of the scattering to the total extinction, shows low values. ~~For large particles the scattering of radiance into the line of sight is the most important mechanism. Since the real part exhibits a step-like structure, the simulated spectra for large NAT particles show this step, too. Medium size particles have contributions of both mechanisms with different proportions depending on the size of the particles. Thus, the shape of the simulated spectra resemble a combination of both parts (real and imaginary) of the refractive index.~~ With increasing median radius of the NAT particles the scattering becomes more and more important. This can be seen by the increase of the SSA, which for large particles then can exceed 0.5, i.e. the scattering increasingly accounts for more than half of the total extinction. As a consequence the peak shifts to smaller wavenumbers with increasing particle size until it transforms to a step-like signature (see Fig. 1 and Fig. 2 b)).

The spectral feature with all its versions in the region 810 – 820 cm^{-1} is a unique signature that only occurs in the presence of NAT PSCs and will be used for the detection of ~~such type of~~ NAT PSCs. Other PSCs consisting of STS or ice do not show such a feature as exemplarily shown in Fig. 1 for two examples with light blue (STS) and dark blue (ice) colours. In contrast to the other PSC types ice shows the largest relative difference between the region 832.0 – 834.0 cm^{-1} and the second spectral range of our simulations (940 – 965 cm^{-1}). Only NAT PSCs consisting of particles with very small radii (< 1.0 µm) can also achieve large differences. This spectral behaviour in the case of ice will further be used to detect ice PSCs.

3.2 Detection of NAT

3.2.1 Unimodal pure NAT

The detection of clouds using infrared limb spectra typically uses the cloud index (CI) (e.g Spang et al., 2001, 2002, 2008). The CI is the radiance ratio between a spectral region dominated by CO_2 at around 792 cm^{-1} and a second spectral region dominated by aerosol or cloud particles at around 833 cm^{-1}. For the analysis of the airborne observations by CRISTA-NF we used the two windows 791.0 – 793.0 cm^{-1} (micro window MW1) and 832.0 – 834.0 cm^{-1} (MW2). Because of the different viewing geometries and instrument properties, the first window is smaller defined than that typically used for satellite observations (Spang et al., 2008). In cloud free conditions the CI value (MW1/MW2) is typically large (around 10). When clouds or larger aerosol loads are in the line of sight of the instrument the CI significantly drops to smaller values depending on the optical thickness of the cloud. The MWs used for the CI and all following indices are marked with gray bars in Fig. 1. Additionally, all indices are summarised in Tab. 4.

The detection of NAT particles inside clouds is based on the characteristic spectral behaviour in the region 810 – 820 cm^{-1}. In former studies a NAT index, the radiance ratio between the spectral region of the typical NAT feature (819 – 821 cm^{-1}) and the region of the CO_2-peak (788 – 796 cm^{-1}), was introduced to detect PSCs containing small NAT particles (e.g Spang and Remedios, 2003; Höpfner et al., 2006; Spang et al., 2012, 2016, 2018). Here, we define the NAT index-1 as the radiance ratio between the two regions 819 – 821 cm^{-1} (MW3) and 791 – 793 cm^{-1} (MW1) and use the same smaller window in the region of the CO_2-peak as for the CI. In a scatter plot of the NAT index-1 versus the CI spectra simulated for small NAT particles separate from spectra simulated for larger NAT particles and other types of PSCs (Fig. 3 a)). Note here, that there is sometimes an overlap of the data points for adjacent radii. This is also the case in the other scatter plots. Nearly all simulations with NAT particles < 3 µm lie above the region of the simulations for STS and ice clouds, which is marked by the solid ~~black~~ red line. Thus, NAT particles within this size range can be detected and discriminated using NAT index-1.

In order to detect PSCs containing larger NAT particles and to make the estimation of the size range of the particles more distinct we introduce two new NAT indices here. The NAT index-2, which is defined as the radiance ratio between 815 – 817 cm^{-1} (MW4) and 791 – 793 cm^{-1} (MW1), focuses on the shifted NAT feature that occurs for larger particles than that producing the non-shifted feature. Figure 3 b) shows the scatter plot of the NAT index-2 versus the CI. In contrast to the NAT index-1 now the results for PSCs with larger NAT particles (up to 4 µm) also lie above the simulations for STS and ice (~~black~~ red separation line). Additonally, for different particle median radii the distance to the separation line changes when going from NAT index-1 to index-2 in an opposite way. In the case of very small particles the distance becomes smaller as the spectral region used for the detection moves away from the center of the typical NAT peak. For larger particles the behaviour is opposite and the distance enlarges as the spectral region moves to the center of the shifted NAT peak. This opposite behaviour can be seen in Fig. 3 c) where the difference between NAT index-1 and index-2 is shown on the y-axis. It is obvious that the simulations for the two smallest radii (0.5 and 1.0 µm) behave opposite to the simulations for larger radii.

Lastly, we introduce NAT index-3, which is defined as the radiance ratio between 810 – 812 cm^{-1} (MW5) and 825 – 827 cm^{-1} (MW6), to detect PSCs containing even larger NAT particles. This ratio enables the discrimination of a step-like feature from a peak and a more or less constant radiance in the complete spectral range as it is the case for STS and ice. Figure 3 d) shows the scatter plot of NAT index-3 against the CI. The simulation results for small NAT particles (≤ 1.0 µm) have a NAT index-3 smaller than for the simulations results for STS and ice. A large part of the simulation results for larger NAT particles show a NAT index-3 that is larger than for the simulation results for STS and ice. By using this ratio also NAT particles with radii > 4 µm separate from the other simulation results and are consequently detectable.

In total the three different NAT indices enable the detection of PSCs containing NAT particles and allow for a classification of the NAT particles in different size regimes. The detection and discrimination of NAT can be divided into three different cases: Case-1 (small NAT): Detection of NAT using NAT index-1 and the difference NAT index-1 – index-2 is above the separation line; Case-2 (medium NAT): Detection of NAT using NAT index-2 and the difference NAT index-1 – index-2 is below the separation line; Case-3 (large NAT): No Detection of NAT using NAT index-1 and index-2 (both below separation line), but the NAT index-3 is above the separation line. Figure 4 shows the proportion between the ~~detected NAT~~ spectra detected as NAT influenced and the cloud spectra (spectra below a certain CI threshold) in each size bin of the simulations (0.5 – 8.0 µm) colour coded for the three different cases. In panel a) of Fig. 4 only observations with a CI below 5.0 are taken into account. Obviously, in case-1 (yellow colour) only NAT particles with a median radius of 0.5 or 1.0 µm are detected. The detection results in case-2 (orange colour) go from 1.5 µm up to 4.0 µm and the results in case-3 (yellow colour) all show median radii larger than or equal to 2.5 µm, whereby the radius 2.5 µm only occurs in a very small amount. Thus, the different cases all represent a specific size regime with no or little overlap to the other cases. Especially, the very small NAT particles (0.5 and 1.0 μm) can be completely distinguished from the particles with other median radii, since all of the detected spectra in this size range fall into case-1. The other two cases have overlap with each other.

The total detection capacity with respect to the simulations is also very good. For median radii up to 6.0 μm nearly all spectra that have been detected as cloud spectra can be detected as spectra influenced by NAT particles. Only for 2.5 and 3.0 μm a few cloud spectra cannot be identified as NAT spectra. These spectra all have a larger CI value ($>$ 3.0, optically thinner) and for larger CI values the separation between NAT and the other PSC types degrades (compare Fig. 3). Thus, a small part of the cloud spectra influenced by NAT cannot be distinguished from STS and ice. When the CI threshold value is reduced to 3.0, the detection itself and also the separation between the different size regimes improves, as shown in Figure 4 b). Now all spectra for median radii up to 6.0 μm are identified as NAT. Additionally the separation between the different sizes is now better and case-3 only detects radii $\geq$ 3.5 μm. Independent of the CI threshold value only a part of the simulations for the largest median radius of 8.0 μm are detected as NAT (CI $<$ 5.0: $\sim$ 30%; CI $<$ 3.0: $\sim$ 40%). This is caused by the decreasing magnitude of the radiance decrease from 811 cm^{-1} to 826 cm^{-1} for increasing median radius (see Sect. 3.1). The improvement of the detection and discrimination when using a CI threshold of 3.0 shows that it is not advisable to use a larger threshold when analysing observations. According to the different size ranges of the three cases, the cases are hereafter denoted as small NAT (sNAT: $\leq$ 1.0 μm), medium NAT (mNAT: 1.5 – 4.0 μm), and large NAT (lNAT: $\geq$ 3.5 μm). Compared to the former method where only the NAT index-1 is used (e.g. Spang and Remedios, 2003; Höpfner et al., 2006; Spang et al., 2012, 2016, 2018) our new approach with three NAT indices enables an improved detection capacity as more NAT clouds can be detected. For our simulations the improvement is about a factor of 1.78 (approximately 190000 cloud spectra identified as NAT with all new indices and about 108000 spectra identified as NAT when only using index-1) for a CI $<$ 3.0.

3.2.2 Influence of tropospheric clouds

The influence of tropospheric clouds was intensively studied during the analysis of the radiative transfer simulations for various PSC situations for the MIPAS-Env satellite instrument (Spang et al., 2012, 2016) and the results can be transfered to here. A tropospheric cloud below the PSC mainly influences the absolute radiance values where the cold tropospheric cloud leads to lower overall radiance values. The appearance of the spectral signature (typical peak, shifted peak, or step-like behaviour) in the region 810 cm^{-1} to 820 cm^{-1} remains nearly unchanged. Simulations by Woiwode et al. (2019) also showed these effects. A similar effect can also be seen in our simulations. The absolute radiances in each spectrum change significantly for the different simulated extinctions, but they do not strongly affect the overall shape of the NAT signature. For extinctions the dependency on particle size is dominating. Thus, extinction and tropospheric clouds alter absolute radiance values but introduce only little changes of the spectral features. As our detection method is based on colour ratios, i.e. relative effects, the change of the absolute radiance values does not significantly influence the analysis. Especially in the case of STS or ice, which define the separation lines (see Fig. 3), the data points in the scatter plots only slightly shift along the correlation lines/regions for the specific PSC type. Thus, the separation lines are still valid in such cases.

3.2.3 Mixed NAT/STS clouds

We additionally simulated mixed NAT/STS clouds to evaluate the influence on the spectra and especially the performance of our classification into different size regimes. Here, we only simulated a subset of all possible combinations, as the spectral behaviour for each median radius is very similar independent of e.g. the bottom altitude of the cloud or the thickness (see Sect. 2.4).

If STS is present in addition to NAT, the relative magnitudes of the spectral features caused by NAT particles get smaller and therefore the separation between these mixed clouds and STS is also restricted compared to a pure NAT cloud. Figure 5 a) shows example spectra for PSCs of pure NAT (solid lines in red for 0.5 μm and blue for 1.0 μm) and PSCs with the same NAT and additionally STS (dashed lines) to illustrate this effect. In a scatter plot of the NAT indices versus the CI (compare Fig. 3 a) and b)) the simulation results for the NAT/STS mixtures are closer to the separation line or even below compared to pure NAT. When the NAT detection and classification procedure (described in the previous subsection) is applied to the simulation results for the mixed clouds, the good discrimination between the small and medium size particles remains. This discrimination relies on the difference of NAT index-1 and index-2, where both indices are influenced in the same way. Therefore, the sign of the difference remains the same because this depends on the position of the spectral peak, which is not affected by the additional STS (see Fig. 5 a)). For a CI value below 3.0 about 97.5% of the simulated cloud spectra with median radii 0.5 and 1.0 μm are correctly detected as sNAT and only about 0.3% are wrongly detected as mNAT (the remaining 2.2% are not detected as NAT). In some cases STS completely masks the spectral features caused by NAT and NAT is not detectable any more. However, for a CI value below 3.0 more than 90% of the cloud spectra can still be identified as containing NAT in the entire simulated size range. ~~This value of 90%~~ The proportion typically decreases with increasing ~~CI~~ median radius, i.e. more NAT influenced spectra at 3.0 μm are missed than at 0.5 μm, and also will decrease with increasing STS volume density or decreasing HNO_3 VMR inside the PSC. In a nutshell, in mixed STS-NAT-clouds ~~less~~ fewer scenarios are identified as containing NAT, because the STS reduces the amplitude of the characteristic NAT signature. But, if a scenario of our simulations was classified as NAT, the size attribution remains as reliable as in the pure NAT scenarios.

3.2.4 Bimodal NAT clouds

In addition, we also simulated PSCs using bimodal NAT particle distributions with a main focus on the small and medium size particles and the separation between those. Here, also a subset of all possible combinations was simulated (see Sect. 2.4).

The spectra simulated for the bimodal NAT particle size distributions are typically some kind of mixture of the spectra for the corresponding unimodal distributions, thereby the HNO_3 VMR ratio plays an important role. Figure 5 b) shows an example for a spectrum simulated for a bimodal NAT particle distribution (black line). The HNO_3 VMRs were 5 ppbv in each mode with median radii of 2.5 μm and 6.0 μm. The two corresponding spectra for the unimodal size distributions are shown in red and blue, respectively. Obviously, the spectrum for the bimodal size distribution is a mixture of the other two. When the HNO_3 ratio for both modes is changed to 70/30 or 30/70 the spectrum looks more like the spectrum for that unimodal size distribution that dominates the bimodal distribution because of more HNO_3 in the corresponding size range.

We applied our classification procedure also to these simulations for bimodal size distributions with the following results. When the first mode dominates (70% HNO_3), nearly all cloud spectra simulated for a median radius of 0.5 or 1.0 μm are still detected as sNAT (about 99% sNAT and 1% mNAT), and thus classified correctly. All spectra that are identified as cloud (CI < 3.0) are also identified as NAT containing PSCs. For a HNO_3 ratio of 50/50 or 30/70 the influence of the second mode increases such that more and more spectra are detected as mNAT and a small part as lNAT. In the case of the ratio 50/50 about 50.5% are classified as sNAT and 49.5% as mNAT and for a ratio of 30/70 21% are classified as sNAT, 77% as mNAT, and 2% as lNAT. When combined with larger NAT particles in the second mode ($\geq$ 4 μm) a part of the cloud spectra (CI < 3.0) are not detected as NAT because neither a spectral peak nor a step-like behaviour can be detected (50/50: 0.5% and 30/70: 10%). However, these cases are only a few percent of all cloud spectra in our simulations. When the first mode has a median radius between 1.5 – 2.5 μm about 99% of the simulated spectra are identified as mNAT (1% lNAT, when the median radius in the second mode is 5.0 or 6.0 μm) independent of the ratio of the HNO_3 VMRs. Furthermore, only a few per ~~mille~~ thousand of the spectra identified as clouds cannot be classified as NAT containing PSCs. In total, our new classification scheme delivers very reasonable results even in the case of bimodal NAT particle size distributions.

3.3 Detection of ice

The detection of ice uses the fact that in the presence of ice a large radiance decrease from about 833 cm^{-1} to 949 cm^{-1} can be observed (compare Fig. 1). This clear decrease is only observed in the case of ice or in the presence of very small NAT particles. Spang et al. (2012, 2016) used this spectral behaviour to detect ice clouds in satellite measurements of MIPAS-Envisat. The authors used the brigthness temperature (BT) difference between the two spectral regions. Here, we adopt the method for the CRISTA-NF observations. Because of the different viewing geometry, spectral resolution and the different definition of the CI for the two instruments, the separation lines have to be newly defined. The spectral regions used for the BT difference are 832.0 – 834.0 cm^{-1} (MW2) and 947.5 – 950.5 cm^{-1} (MW7). In a scatter plot of the BT difference against the CI, the simulated ice spectra clearly separate from other particle types (Fig. 6). Obviously, spectra that are influenced by ice clearly separate from STS and nearly all NAT particles when the cloud is optically thick enough (low CI). For larger CI values the separation gets smaller. The only particle type that can produce similar values of the BT difference are very small NAT particles with median radii of 0.5 μm (yellow colours in Fig.6 a)), but these particles can be safely filtered out with the method described before in Sect. 3.2. Consequently, the BT difference is a very robust method to detect ice particles in PSCs.

3.4 Detection of STS

~~Unfortunately,~~ The spectra for STS show neither a local spectral feature like the spectra for NAT nor a broadband spectral feature such as the spectra for ice. Thus, the detection of STS can not be achieved by using a unique spectral behaviour. In practice the detection procedure is as follows. Firstly, the NAT detection methods are used to detect observations of NAT particles and to distinguish between the three size regimes. Secondly, the BT difference method is applied to the observations to detect ice. Finally, the observations inside PSCs that are neither detected as NAT nor as ice are categorised as STS. It is not necessarily the case that the spectra categorised as STS are solely influenced by STS. It is possible that NAT or ice also were present in the PSC but the additional amount of STS was enough to minimise the spectral features such that NAT or ice is not definitely detectable any more. Furthermore, the small amount of very large NAT particles that cannot be distinguished from STS and ice will also fall in the category STS.

3.5 Bottom altitude of the PSCs

Further important quantities with respect to cloud detection are the vertical thickness and the position of the cloud defined by the top and bottom altitude. Here, we present a method to determine the bottom altitude of the observed cloud. The cloud index, which is used to detect optically thick conditions caused by clouds (or aerosol), shows characteristic vertical changes in the presence of clouds. These changes are used for the detection of the cloud bottom altitude.

The left panel of Fig. 7 shows examples of CI altitude profiles for clouds with different vertical thicknesses. When the complete cloud is located below the flight altitude (yellow colour) the CI largely drops to low values when entering the cloud from above (or slightly above because of the FOV). In the case the flight altitude is inside the cloud the CI is already low at flight altitude. Then the CI typically further decreases with decreasing altitude inside the cloud and the minimum CI value is reached close to the bottom altitude. Only in some cases when the vertical thickness is larger (4 km or 8 km) the CI minimum can be located somewhere inside the cloud. When leaving the cloud the CI increases again. These vertical changes of the CI can be best illustrated with the gradient of the CI (right panel in Fig. 7). Slightly above the cloud top the vertical gradient maximises and slightly below the cloud bottom the gradient reaches its minimum value. In contrast to the CI minimum, where larger deviations to the cloud bottom can occur, the minimum of the gradient is always slightly below the real bottom altitude of the cloud.

Figure 8 summarises the results for the simulated clouds with a bottom altitude below flight altitude. In the case of the CI minima (full circles) there are sometimes larger deviations from the real bottom altitude when the cloud is vertically thick (red and light blue full circles). The CI gradient minima (full diamonds) are always located close to the real bottom altitude, at the first or the second measurement below. The possibility to observe the gradient minimum at the second measurement below the cloud increases with decreasing altitude of the cloud, because the vertical extent in metres of the FOV is larger at lower altitudes. In our simulations this occurs only at bottom altitudes of 13.0 and 14.0 km. In summary, the CI minimum and the gradient minimum enclose the real bottom altitude. A large gap between the two minimum values indicates the observation of a cloud with a larger vertical thickness.

There are further restrictions for the determination of the bottom altitude. ~~Firstly, when the cloud is optically too thick, a vertical change of CI can hardly be seen anymore.~~ In some cases the observations run into saturation and the CI values below the cloud bottom altitude converge at a low value. Additionally, in some other situations the CI values below the bottom altitude only show a linear increase and not the larger change directly below the bottom altitude. In both cases ~~Therefore,~~ the CI minimum and the gradient minimum cannot sufficiently be determined and used for the detection of the bottom altitude ~~of an optically thick~~ of the cloud. An effective way to sort out possibly affected observations is the use of a threshold value. A CI minimum below 1.25 we derived from the simulations. ~~A CI minimum value of 1.2 serves as a good threshold.~~ Such low values of CI only occur for a part of the ice clouds simulated here ~~but not for~~ (typically for largest volume densities of 50 and 100 $\mu\mathrm{m}^3/\mathrm{cm}^3$; with increasing vertical thickness also some simulations with 5 and 10 $\mu\mathrm{m}^3/\mathrm{cm}^3$ were affected) and for a few of the NAT and

STS clouds with large HNO_3 VMRs (≥ 11 ppbv) or volume densities ($\geq 5\ \mu m^3/cm^3$) combined with a large vertical thickness (≥ 4 km). Secondly, when the cloud is optically and vertically thin, the location of the cloud bottom is not detectable as well. In order to select only clouds that are optically thick enough for detection we used only simulation spectra with CI < 5.0. Furthermore, more special situations can be considered, PSC only above flight altitude and layered PSCs. When the PSC is located above the flight altitude the CI typically increases with decreasing altitude from flight altitude downwards, because the length of the line of sight inside the PSC decreases also. Thus, there is not the typical decrease of the CI to a local minimum, but rather a continuous increase from a rather low CI value compared to clear air at flight altitude. Both, the CI and the CI gradient, typically show the lowest values at the points closest to the flight altitude. In the case of layered PSCs, where PSCs of different type are lying above each other, the results depend on the optical thickness of the different layers. On the one hand, the CI gradient minimum is still located at the bottom of the complete PSC, when the lower layer is optically thick enough and the transition to the cloud free atmosphere shows the largest increase in CI. On the other hand, when the lower layer is optically very thin, it can occur that the CI gradient minimum is located directly below the upper layer. In this case the transition from the upper layer to the lower layer leads to a larger increase in CI than the transition from the lower layer to the cloud free atmosphere.

4 Application to the CRISTA-NF measurements

This section shows the application of the methods derived from the simulations to observations by the CRISTA-NF instrument for all flights during RECONCILE, where PSCs were observed. These PSC observations were carried out during the first five flights between 17.01.2010 to 25.01.2010. For one selected flight (local flight 3: 22.01.2010) we additionally show more details of the results to demonstrate the capability of the instrument and the methods. ~~We show results for the detection of the bottom altitude and the detection and discrimination of PSCs exemplarily for the RECONCILE local flight 3, which took place on 22.01.2010. The flight started in Kiruna (Sweden) and the whole flight was located northward of Kiruna inside the polar vortex.~~

4.1 Analysis of the CRISTA-NF measurements

We applied the dection methods for NAT and ice using the NAT indices and the BTD to the measurements by CRISTA-NF for flight 1 – 5. The results for the different scatter plots are shown in Fig. 9 a) – e). Note here, for flight 2 – 5 the measurements were filtered so that only measurements inside PSCs have been taken into account (more details see Sect. 4.2). In the case of flight 1 this filtering was not possible as many profiles show very low CI values (see Sect. 3.5) and, thus, simply all measurements between flight altitude and 14 km are shown. The observations separate into two different situations. First, during flight 1 a clear signal of ice was detected, which can been seen in Fig. 9 e), and no indication of NAT. For all NAT indices vs. CI the data points stay below the separation lines in the same way as the simulation results for ice (see Fig. 3). This shows the good correspondence between simulations and observations. The ice observation is supported by ECMWF data (not shown), which show temperatures low enough for ice formation above the flight altitude at about 20 km and above, and

CALIPSO observations that show ice PSCs above 20 km a few hours before the flight (personal communication: M. Pitts). Thus, CRISTA-NF observed the ice PSC from below. As ice PSCs are typically optical thicker than other PSCs, this explains the lower values of CI observed during this flight. Second, the flights 2 – 5 all show signatures of NAT (see Fig. 9 a) and b)). As the differences between NAT index-1 and index-2 are below the separation line (see Fig. 9 c)), these observations are categorised as mNAT. The difference of the spectra for these two PSC types is additionally illustrated in Fig. 9 f) with example spectra for flight 1 (blue colours) and flight 3 (red colours). They are scaled for better comparability. Obviously, the spectra in flight 3 show a shifted NAT peak and the spectra in flight 1 a large negative gradient towards larger wavenumbers, which clearly shows the influence by ice (compare Fig. 1).

Because of the strong radiance enhancement caused by the clouds, the dominating uncertainty is the relative uncertainty (noise uncertainty) of the measurements, whereas a systematic uncertainty (e.g. an offset) plays a minor role. The relative uncertainty for the radiances typically observed during atmospheric measurements is about 1–2% for CRISTA-NF (Schroeder et al., 2009). Because of the calculation of ratios, the relative error can add up, but is still only a few percent. In the worst case the maximum uncertainty is about 2-4%. For the analysis of the PSC observations this has a different effect depending on the CI and the NAT-index. For smaller values of the CI and NAT indices the resulting absolute uncertainties of these quantities determined from the relative uncertanties are smaller than for larger values. Thus, the methods work better for smaller CI values. This suggests to use a threshold value for the CI and to only analyse observations with a CI below this threshold as it was done in Sect. 3.2. Furthermore, the same spectral windows are used for CI and NAT index-1/2. In this case some of the uncertainty will cancel, as the data points will shift similar to the correlation regions/lines, i.e. a smaller CI (because of a smaller randiance in the CO_2-window) will be accompanied by a larger NAT index and vice versa. However, many observations, especially for flight 3 and 5, show deviations from the separation line larger than a few percent and a clear separation between ice and NAT (see Fig. 9 a), b)). Furthermore, they show a compact correlation and not a spread as it would be expected for large noise errors.

4.2 Detailed Results for flight 3

We show more detailed results for the detection of the bottom altitude and the detection and discrimination of PSCs exemplarily for the RECONCILE local flight 3, which took place on 22.01.2010. The flight started in Kiruna (Sweden) and the whole flight was located northward of Kiruna inside the polar vortex.

4.2.1 Bottom altitude

During the RECONCILE local flight 3 the aircraft flew through PSCs. Thus, the CRISTA-NF instrument made measurements inside PSCs during a large part of the flight. The behaviour of the CI and the CI gradient can now be used to detect the bottom of the PSCs. Figure 10 shows the CI and the CI gradient for two selected altitude profiles that have been measured inside PSCs. These two profiles show the behaviour as expected from the simulations. In case of profile 102 (right panel in Fig. 10) the CI becomes smaller from flight altitude downwards as long as the measurements are inside the cloud (compare red and yellow profile of CI in Fig. 7). The CI gradient shows the largest negative value one sampling step below the CI minimum. According to the simulation results the CI gradient minimum is located below the cloud whereas the CI minimum is located inside the cloud. Thus, in this example an accurate detection of the bottom altitude is possible (profile 102: $\sim$17.3 – 17.4 km). In the case of profile 80 the behaviour of CI and CI gradient is very similar. Only the altitude difference between the CI minimum and the CI gradient minimum is larger than only one sampling step (profile 80: $\sim$17.2 – 17.5 km). This can be caused by two effects. Firstly, the PSC is inhomogeneous and this causes the increase of the CI above the CI gradient minimum which is supposed to be located directly below the PSC. Secondly, in the case of vertically largely extended clouds this behaviour is also observed in the simulations (compare Fig.7 blue curves). If the vertical extent is responsible for the difference between the two minima, this would suggest that the vertical exten~~d~~t is larger than 2 km. However, the difference between the two minima is only about 300 m. Thus, the detection of the bottom altitude, which is located between these two points, is still very accurate.

Figure 11 a) shows the cross section of the CI for the complete flight. During the middle section of the flight the aircraft crossed PSCs as can be seen by the low CI values (blue colours) at and directly below the flight altitude. Beneath this region the CI values are larger again, which indicates cloud free conditions below the PSCs. The green and the magenta line in Fig. 11 a) mark the CI minima and the CI gradient minima, respectively. Only profiles where both minima could sufficiently be determined are considered. Similar to the results for the two selected profiles (compare Fig. 10) the two minima are primarily located in the region between 17 and 17.5 km. Thus, for most profiles a good estimate of the bottom altitude of the cloud is achieved.

4.2.2 PSC classification

~~The measurements are now analysed with respect to the PSC type using the methods described in Sect. 3.~~ During a large part of the flight numerous spectra below the bottom altitude of the cloud (see green and magenta lines in Fig. 11 a)) would be detected as PSC influenced spectra. This is expected as a large part of the line of sight (LOS) is still inside the PSC and, thus, the spectral features caused by the PSC particles are visible in the spectra. Since the cloud bottom height was determined by the CI gradient method, we restricted the analysis of the altitude range between flight altitude and the CI gradient minima. Figure 11 b) shows the cross section of the detected PSC types. Additionally, only spectra with a CI value below 3.0 are considered (Fig. 11 b)). During the complete flight only medium sized NAT and STS were observed (orange and light blue colours in Fig. 11 b)). Figure 12 shows example spectra inside the PSCs at about 12:10 UTC, which show a shifted NAT feature at about 816 cm^{-1}, and thus a classification as mNAT is expected. The new method reliably detects spectra showing such a shifted NAT feature. Most of the observations detected as STS are located in the second half of the PSC observation from the flight altitude downwards. This is also in accordance with the spectra that have been measured in this region. These spectra (see Fig.12) show a clear shifted NAT feature only at altitudes a few hundred metres below flight altitude. Directly below the flight altitude the NAT feature can hardly be seen. This does not necessarily mean that no NAT was present in this altitude region, but the STS contribution to the measured radiances was that large, thus all other particle type signatures were masked out. Additionally, the CI values in this region are lower directly below flight altitude (compare Fig. 11 a)) compared to the first part of the PSC. In addition to the smaller distance between the CI minima and the gradient minima in the second part of the PSC this suggests that the vertical extent of the cloud is smaller compared to the first part or that the PSC is optically thinner.

In summary the methods derived in Sect. 3 are able to give a complete picture of the observed PSC. The PSC and the bottom altitude of the cloud are clearly detected and the new and improved detection method enables the classification of medium size NAT particles and STS during RECONCILE flight 3.

5 Discussion

Small NAT particles cause a distinct spectral peak in infrared limb emission spectra at about 820 cm^{-1}. This peak has already been observed in satellite measurements since the 1990's (Spang and Remedios, 2003; Höpfner et al., 2006). We showed with our simulations that the appearance of the NAT feature changes with changing particle size. The spectral peak (small NAT) transforms to a shifted peak (medium NAT) and, finally, to a step-like behaviour of the spectrum (large NAT) with increasing median radius of the particle size distribution. This change is related to the different proportions to which scattering and absorption/emission contribute to the total radiance (see also Woiwode et al., 2016).

The ~~different spectral features~~ change in the appearance of the feature can be used to distinguish between different size regimes. Our new approach enables the differentation between small NAT (0.5 – 1.0 $\mu\mathrm{m}$), medium NAT (1.5 – 4.0 $\mu\mathrm{m}$), and large NAT ($\geq$ 3.5 $\mu\mathrm{m}$). In contrast to the former method where only one NAT index is used (detection of NAT $<$ 3.0 $\mu\mathrm{m}$) (see Spang and Remedios, 2003; Höpfner et al., 2006; Spang et al., 2016) this improved method leads to a larger detection capacity as more NAT containing clouds can be detected. A part of the medium sized particles (those when only NAT index-2 is above the separation line) and the complete size range of large NAT particles are not detected with the former method. Probably this improvement will diminish the discrepancy between NAT cloud observations by MIPAS-Envisat and the CALIOP (Cloud-Aerosol Lidar with Orthogonal Polarization) instrument onboard CALIPSO (Cloud-Aerosol Lidar and Infrared Pathfinder Satellite Observation; Pitts et al., 2018) in the Northern hemisphere, where much more NAT was observed by CALIOP and the agreement for the NAT observations by both instruments is only 18% (~~the difference in the Southern hemisphere is much smaller~~the agreement for NAT observations in the Southern hemisphere is much better with about 73%)(Spang et al., 2018; Tritscher et al., 2020). Consequently, this would conclude a larger probability for the formation of NAT clouds with medium to large radii for the Northern hemisphere compared to Southern hemisphere conditions, which highlights a link to different formation mechanisms and meteorological conditions fostering the formation of large or small NAT particles.

The derived methods can easily be adopted to analyse other observations like that of MIPAS-Envisat, as the spectral behaviour in general is the same. The separation lines would need to be adjusted, because different instruments have different spectral properties and viewing geometries. Thus, the new NAT detection method can be transfered to MIPAS-Envisat, but a set of simulations is necessary to do this. In the case of the ice detection we sucessfully transferred the method used for MIPAS-Envisat (e.g. Spang et al., 2016) to the airborne geometry of CRISTA-NF and refined the separation lines.

In recent publications by Woiwode et al. (2016, 2019) a special step-like behaviour of infrared spectra in the presence of NAT particles was intensively analysed and the authors simulated the observed spectra by the presence of large aspherical NAT particles. Woiwode et al. (2019) showed the large shoulder-like signature at about 820 cm^{-1} and flat radiance behaviour afterwards, which they called a hockey-stick signature, for an example observed by MIPAS-Envisat. The authors assigned this behaviour to be characteristic for large aspherical NAT particles and developed a detection method for this type of spectrum. The main criteria used for the detection are a difference in the integrated radiance between the window 817.5 – 818.5 cm^{-1} and 833.0 – 834.0 cm^{-1} above a certain value (to detect the step or shoulder) and a difference in the integrated radiance between the window 833.0 – 834.0 cm^{-1} and 960.0 – 961.0 cm^{-1} below a certain value (to detect the flat behaviour at larger wavenumbers). Our simulations agree at the point that large spherical NAT particles (with unimodal distribution) typically show a step-like behaviour but a decrease in the radiance towards larger wavenumbers (compare Fig. 1 reddish colours and Fig. 5 b) blue line), and therefore do not show this hockey-stick signature. But some of our simulations for the bimodal NAT particle size distributions show this typical behaviour. The spectrum in Fig. 5 for the bimodal NAT particle size distribution (black line) exhibits no ~~decrease~~ difference in radiance from about 833 to 960 cm^{-1}. Furthermore, the step or shoulder is more pronounced compared to the spectrum for the unimodal size distribution (blue line) and slighty shifted towards larger wavenumbers. Therefore, the radiance decrease from 818 to 833 cm^{-1} increases. In our opinion, ~~the spectral behaviour presented here is very similar to the spectra of without using aspherical NAT particles at all.~~ this spectrum will probably fullfil all criteria used for the detection of large aspherical NAT particles as described in Woiwode et al. (2019). This suggest that large aspherical NAT particles are not necessarily the only possibility to observe such a kind of spectrum or spectral signature that fullfil the criteria of the detection method. Thus, the spectrum alone is possibly not enough to definitely detect aspherical NAT particles. But a complete picture of the situation involving infrared emission spectra, FSSP (Forward-Scattering Spectrometer Probes; Molleker et al., 2014) observations of the particle size distribution, and information on the $\mathrm{HNO_3}$ budget together will presumably be sufficent to make a clear decision. For single spectra this has been done by Woiwode et al. (2016, 2019) and in these special cases aspherical NAT particles led to the best results.

~~Unfortunately,~~ As the differences used in the detection scheme by Woiwode et al. (2019) rely on absolute differences.~~, which are not applicable for CRISTA-NF, because of the viewing geometries and spectral properties of the instruments.~~ and as CRISTA-NF and MIPAS-Envisat have different viewing geometries etc., the absolute radiance values and therefore the differences are not comparable. Thus, the detection method cannot be applied to CRISTA-NF observations or simulations. In order to analyse the detection scheme by Woiwode et al. (2019) in more detail simulations for the MIPAS-Envisat instrument are necessary, which is beyond the scope of this paper. ~~However, the simulations for the CRISTA-NF instrument clearly show the effects of bimodal NAT particle size distributions on the infrared spectra and the possibility to obtain a hockey-stick signature.~~ However, our simulation results demonstrate that spherical particles can produce all the different appearances of the NAT feature (typical feature, shifted feature, step-like behaviour) including those previously attributed to highly aspherical NAT. We think that this is an important point to consider as it implies that IR limb emission measurements alone are not sufficient to prove the existence of aspherical NAT, in particular for cases without additional information on the atmospheric state and cloud particle size distribution. Our approach of grouping the NAT particles into 3 size bins based on the spectral signature we do not consider affected by the particle shape for the following reasons. The small particles ($< 3\ \mu$m) are considered not or only slightly aspherical. For our approach we used the term 'small' for particle size distributions with median radii $\leq 1.0\ \mu$m. Also Woiwode et al. (2019) use the method by Höpfner et al. (2006), which is based on simulations using spherical particles, to detect these small particles. Further, a substantial fraction of our 'medium' size group (median radii $\leq 4\ \mu$m) can be considered nearly aspherical. The shifted NAT signature reported by Woiwode et al. (2016) for highly ashperical NAT is bi-modal with median radii of 2 and

4.8 μm, where the latter is dominating the signal. This means that the shifted NAT signature that so far was solely attributed to the asphericity, has only been observed in the presence of larger NAT particles. Further, Woiwode et al. (2019) (Fig. 1) show that for median radii $\geq 5.0\,\mu$m a step-like NAT-feature can be observed. Hence, our result that the shift of the NAT signature is associated with NAT particle size is in line with the results of Woiwode et al. (2016, 2019). Due to particle asphericity our size bin boundary between 'medium' and 'large' has uncertainties and the numbers given here are valid under the assumption of spherical particles.

6 Summary and conclusions

We performed a large set of radiative transfer simulations of infrared limb emission spectra in the presence of polar stratospheric clouds of different types (NAT, STS, ice). All simulations have been performed for the viewing geometry and spectral properties of the CRISTA-NF instrument. These simulations build a new data base that is used for the analysis of PSC spectra to develop and refine detection and discrimination methods.

We showed with our simulations that the NAT feature changes from a spectral peak at 820 cm^{-1} (small NAT) to a shifted peak (medium NAT) and, finally, to a step-like behaviour of the spectrum (large NAT) with increasing median radius. Based on this behaviour we developed an improved method to detect NAT particles, which for the first time allows the discrimination of three different size regimes: small NAT (0.5 – 1.0 μm), medium NAT (1.5 – 4.0 μm), and large NAT ($\geq$ 3.5 μm) under the assumption of spherical particles. This new detection method will also improve the analysis of other observations by infrared limb emission sounder such as MIPAS-Envisat. The ice detection method was adopted from former studies (MIPAS-Envisat) and the separation lines were newly defined. Additionally, we developed a new method to detect the bottom altitude of the clouds. This method uses the gradient of the CI, which minimises shortly below the real bottom altitude. As the minimum of the CI itself is located inside the cloud (typically close to the bottom), these two quantities give a good estimate for the bottom altitude. This method can surely be transfered to other cloud observations such as cirrus clouds and aerosol layers and to other airborne instruments measuring in the same wavelength region like e.g. GLORIA (Gimballed Limb Observer for Radiance Imaging of the Atmosphere; Riese et al., 2014). A prerequsite for a sucessful usage of the method is a small FOV like that of CRISTA-NF. Larger FOVs will lead to a larger vertical averaging of the measurements and thus to a ~~minimisation~~ reduction of the detection capabilities. This can already be seen for the CRISTA-NF instrument, where at lower altitudes (14 km and below) the minimum of the CI gradient can move further away from the real bottom altitude.

Finally, we applied the new methods to observations of CRISTA-NF during the RECONCILE local flight 3. The results show a polar stratospheric cloud that has been crossed during the flight by the aircraft and extends downward to about 17 – 17.5 km. The PSC contained NAT particles, which could be classified to be of medium size (1.5 – 4 μm) as in the spectra always a shifted NAT feature has been observed. This shifted feature is ~~safely~~ detected by the new method.

Moreover, using the method developed here a new data set of PSC observations and classification can be obtained. This new data set will help to improve the results of trace gas retrievals in the presence of PSCs by integrating realistic PSC extinction spectra into the retrieval process. Furthermore, the gained data will help to improve the representation of PSCs in model simulations.

Code and data availability. The JURASSIC code is available at https://github.com/slcs-jsc/jurassic-scatter. The simulation results are available at https://datapub.fz-juelich.de/slcs/cloud-spectra/psc-crista-nf/. The CRISTA-NF level 1b data can be obtained by request to the corresponding author.

Author contributions. The setup of the simulations (background atmosphere, cloud scenarios, etc.) was compiled and discussed with all authors CK, SG, and RS. The simulations have been mainly performed by SG and the analysis was mainly done by CK under intensive discussions with all authors. CK wrote the manuscript with contributions of the two other authors SG and RS.

Competing interests. The authors declare that they have no competing interests.

Acknowledgements. The work by Christoph Kalicinsky was funded by the German Science Foundation (DFG) under the grant number 4118/2-1. The authors gratefully acknowledge the Gauss Centre for Supercomputing e.V. (www.gauss-centre.eu) for funding this project by providing computing time through the John von Neumann Institute for Computing (NIC) on the GCS Supercomputer JUWELS at Jülich Supercomputing Centre (JSC). We thank the Canadian Space Agency for access to the ACE-FTS data. We gratefully acknowledge the European Centre for Medium Range Weather Forecast (ECMWF) for proving the ERA-Interim data. We thank C.M. Volk and the HAGAR team for the access to the HAGAR data. We additionally thank M. Diallo for providing the CO_2 data product.

References

Achtert, P., and Tesche, M.: Assessing lidar-based classification schemes for polar stratospheric clouds based on 16 years of measurements at Esrange, Sweden, J. Geophys. Res., 119, 1386–1405, doi:10.1002/2013jd020355, 2014.

Biermann, U.M.: Gefrier- und FTIR-Experimente zur Nukleation und Lebensdauer stratosphärischer Wolken, Ph.D. thesis, Universität Bielefeld, Germany, ISBN 3-89712-212-X, 1998.

Biermann, U.M., Luo, B.P., and Peter, T.: Absorption spectra and optical constants of binary and ternary solutions of H_2SO_4, HNO_3, and H_2O in the mid infrared at atmospheric temperatures, J. Phys. Chem. A, 104, 783–793, doi:10.1021/jp992349i, 2000.

Boone, C.D., Walker, K.A., Bernath, P.F.: Version 3 Retrievals for the Atmospheric Chemistry Experiment Fourier Transform Spectrometer (ACE-FTS), in: The Atmospheric Chemistry Experiment ACE at 10: a solar occultation anthology, edited by: Bernath, P.F., A Deepak Publishing, Virginia, United States of America, 103–127, 2013.

Bullister, J.: Atmospheric CFC-11, CFC-12, CFC-113, CCl_4 and SF_6 Histories., Tech. rep., Carbon Dioxide Information Analysis Center, Oak Ridge National Laboratory, US Department of Energy, Oak Ridge, Tennessee, 2011.

Carslaw, K. S., Peter, T., and Müller, R.: Uncertainties in reactive uptake coefficients for solid stratospheric particles – 2. Effect on ozone depletion, Geophys. Res. Lett., 24, 1747–1750, doi:10.1029/97GL01684, 1997.

Carslaw, K. S., Wirth, M., Tsias, A., Luo, B. P., Dörnbrack, A., Leutbecher, M., Volkert, H., Renger, W., Bacmeister, J. T., Reimer, E., and Peter, T.: Increased stratospheric ozone depletion due to mountain-induced atmospheric waves, Nature, 391, 675–678, doi:10.1038/35589, 1998.

Dee, D.P., Uppala, S.M., Simmons, A.J., Berrisford, P., Poli, P., Kobayashi, S., Andrae, U., Balmaseda, M.A., Balsamo, G., Bauer, P., Bechtold, P., Beljaars, A.C.M., van de Berg, L., Bidlot, J., Bormann, N., Delsol, C., Dragani, R., Fuentes, M., Geer, A. J., Haimberger, L., Healy, S.B., Hersbach, H., Hólm, E.V., Isaksen, L., Kållberg, P., Köhler, M., Matricardi, M., McNally, A.P., Monge-Sanz, B.M., Morcrette, J.-J., Park, B.-K., Peubey, C., de Rosnay, P., Tavolato, C., Thépaut, J.-N. and Vitart, F.: The ERA-Interim reanalysis: configuration and performance of the data assimilation system, Q.J.R. Meteor. Soc., 137, 553–597, doi:10.1002/qj.828, 2011.

Diallo, M., Legras, B., Ray, E., Engel, A., and Añel, J. A.: Global distribution of CO_2 in the upper troposphere and stratosphere, Atmos. Chem. Phys., 11, 3861–3878, doi:10.5194/acp-17-3861-2017, 2017.

Dörnbrack, A., Birner, T., Fix, A., Flentje, H., Meister, A., Schmid, H., Browell, E. V., and Mahoney, M. J.: Evidence for inertia gravity waves forming polar stratospheric clouds over Scandinavia, J. Geophys. Res., 107, 8287, doi:10.1029/2001JD000452, 2002.

Drdla, K. and Müller, R.: Temperature thresholds for chlorine activation and ozone loss in the polar stratosphere, Ann. Geo-phys., 30, 1055–1073, doi:10.5194/angeo-30-1055-2012, 2012.

Dudhia, A.: The Reference Forward Model (RFM), J. Quant. Spectrosc. Radiat. Transfer, 186, 243–253, 2017.

Engel, I., Luo, B. P., Pitts, M. C., Poole, L. R., Hoyle, C. R., Grooß, J.-U., Dörnbrack, A., and Peter, T.: Heterogeneous formation of polar stratospheric clouds – Part 2: Nucleation of ice on synoptic scales, Atmos. Chem. Phys., 13, 10769–10785, doi:10.5194/acp-13-10769-2013, 2013.

Eyring, V., Arblaster, J. M., Cionni, I., Sedlácek, J., Perlwitz, J., Young, P. J., Bekki, S., Bergmann, D., Cameron-Smith, P., Collins, W. J., Faluvegi, G., Gottschaldt, K.-D., Horowitz, L. W., Kinnison, D. E., Lamarque, J.-F., Marsh, D. R., Saint-Martin, D., Shindell, D. T., Sudo, K., Szopa, S., and Watanabe, S.: Long-term ozone changes and associated climate impacts in CMIP5 simulations, J. Geophys. Res.-Atmos., 118, 5029–5060, doi:10.1002/jgrd.50316, 2013.

Fahey, D.W., Gao, R.S., Carslaw, K S., Kettleborough, J., Popp, P.J., Northway, M.J., Holecek, J.C., Ciciora, S.C., McLaughlin, R.J., Thompson, T.L., Winkler, R.H., Baumgardner, D.G.,Gandrud, B., Wennberg, P.O., Dhaniyala, S., McKinley, K., Peter, T., Salawitch, R.J., Bui, T.P., Elkins, J.W., Webster, C.R., Atlas, E.L., Jost, H., Wilson, J.C., Herman, R.L., Kleinböhl, A.,and von König, M.: The detection of large HNO_3 containing particles in the winter Arctic stratosphere, Science, 291, 1026–1031,2001.

Fastie, W.: Ebert Spectrometer Reflections, Phys. Today, 4, 37–43, 1991.

Fischer, H., Birk, M., Blom, C., Carli, B., Carlotti, M., von Clarmann, T., Delbouille, L., Dudhia, A., Ehhalt, D., Endemann, M., Flaud, J. M., Gessner, R., Kleinert, A., Koopman, R., Langen, J., López-Puertas, M., Mosner, P., Nett, H., Oelhaf, H., Perron, G., Remedios, J., Ridolfi, M., Stiller, G., and Zander, R.: MIPAS: an instrument for atmospheric and climate research, Atmos. Chem. Phys., 8, 2151–2188, doi:10.5194/acp-8-2151-2008, 2008.

Glatthor, N., von Clarmann, T., Fischer, H., Funke, B., Grabowski, U., Höpfner, M., Kellmann, S., Kiefer, M., Linden, A., Milz, M., Steck, T., and Stiller, G. P.: Global peroxyacetyl nitrate (PAN) retrieval in the upper troposphere from limb emission spectra of the Michelson Interferometer for Passive Atmospheric Sounding (MIPAS), Atmos. Chem. Phys., 7, 2775–2787, doi:10.5194/acp-7-2775-2007, 2007.

Gordley, L.L., and Russell III, J.M.: Rapid inversion of limb radiance data using an emissivity growth approximation, Appl. Optics, 20, 807–813, 1981.

Griessbach, S., Hoffmann, L., Hoepfner, M., Riese, M., and Spang, R.: Scattering in infrared radiative transfer: A comparison between the spectrally averaging model JURASSIC and the line- by-line model KOPRA, J. Quant. Spectrosc. Radiat. Transfer, 27,102–118, 2013.

Griessbach, S., Hoffmann, L., Spang, R., and Riese, M.: Volcanic ash detection with infrared limb sounding: MIPAS observations and radiative transfer simulations, Atmos. Meas. Tech., 7, 1487-1507, 2014.

Griessbach, S., Hoffmann, L., Spang, R., von Hobe, M., Müller, R., and Riese, M.: Infrared limb emission measurements of aerosol in the troposphere and stratosphere, Atmos. Meas. Tech., 9, 4399–4423, 2016.

Griessbach, S., Hoffmann, L., Spang, R., Achtert, P., von Hobe, M., Mateshvili, N., Müller, R., Riese, M., Rolf, C., Seifert, P., and Vernier, J.-P.: Aerosol and cloud top height information of Envisat MIPAS measurements, Atmos. Meas. Tech., doi:10.5194/amt-13-1243-2020, 2020.

Grossmann, K. U., Offermann, D., Gusev, O., Oberheide, J., Riese, M., and Spang, R.: The CRISTA-2 mission, J. Geophys. Res., 107, 8173, doi:10.1029/2001JD000667, 2002.

Hoffmann, L.: Schnelle Spurengasretrieval für das Satellitenexperiment Envisat MIPAS, JUEL-4207, Forschungszentrum Jülich, Germany, ISSN 0944-2952, 2006.

Hoffmann, L., Spang, R., Kaufmann, M., and Riese, M.: Retrieval of CFC-11 and CFC-12 from Envisat MIPAS observations by means of rapid radiative transfer calculations, Adv. Space Res., 36, 915–921, 2005.

Hoffmann, L., Kaufmann, M., Spang, R., Müller, R., Remedios, J.J., Moore, D.P., Volk, C.M., von Clarmann, T., and Riese, M.: Envisat MIPAS measurements of CFC-11: retrieval, validation, and climatology, Atmos. Chem. Phys., 8, 3671–3688, 2008.

Hoffmann, L., Weigel, K., Spang, R, Schroeder, S., Arndt, K., Lehmann, C., Kaufmann, M., Ern, M., Preusse, P., Stroh, F., and Riese, M.:CRISTA-NF measurements of water vapor during the SCOUT-O3 Tropical Aircraft Campaign, Adv. Space Res., 43, 74–81, 2009.

Hoffmann, L., and Alexander, M.J.: Retrieval of stratospheric temperatures from Atmospheric Infrared Sounder radiance measurements for gravity wave studies, J. Geophys. Res., 114, D7, D07105, 2009.

Hoffmann, L., and Riese, M.: Tomographic Retrievals for High Spatial Resolution Measurements of the PREMIER Infrared Limb Sounder, in: Proceedings of the ESA Living Planet Symposium, SP-686, ESA Publications Division, ESTEC, Keplerlaan 1, 2200 AG Noordwijk, The Netherlands, 2010.

Hoffmann, L., Spang, R., Orr, A., Alexander, M. J., Holt, L. A., and Stein, O.: A decadal satellite record of gravity wave activity in the lower stratosphere to study polar stratospheric cloud formation, Atmos. Chem. Phys., 17, 2901–2920, doi:10.5194/acp-17-2901-2017, 2017.

Höpfner, M., Oelhaf, H., Wetzel, G., Friedl-Vallon, F., Kleinert, A., Lengel, A., Maucher, G., Nordmeyer, H., Glatthor, N., Stiller, G., v. Clarmann, T., Fischer, F., Kröger, C., and Deshler, T.: Evidence of scattering of tropospheric radiation by PSCs in mid-IR limb emission spectra: MIPA-B observations and KOPRA simulations, Geophys. Res. Lett., 29, 1278, doi:10.1029/2001GL014443, 2002.

Höpfner, M., and Emde, C.: Comparison of single and multiple scattering approaches for the simulation of limb-emission observations in the mid-IR, J. Quant. Spectrosc. Radiat. Transf., 91, 275–285, doi:10.1016/j.jqsrt.2004.05.066, 2005.

Höpfner, M., Luo, B.P., Massoli, P., Cairo, F., Spang, R., Snels, M., Di Donfrancesco, G., Stiller, G., von Clarmann, T., Fischer, H., and Biermann, U.: Spectroscopic evidence for NAT, STS, and ice in MIPAS infrared limb emission measurements of polar stratospheric clouds, Atmos. Chem. Phys., 6, 1201-1219, doi:10.5194/acp-6-1201-2006, 2006.

Kalicinsky, C., Grooß, J.-U., Günther, G., Ungermann, J., Blank, J., Höfer, S., Hoffmann, L., Knieling, P., Olschewski, F., Spang, R., Stroh, F., and Riese, M.: Observations of filamentary structures near the vortex edge in the Arctic winter lower stratosphere, Atmos. Chem. Phys., 13, 10859-10871, doi:10.5194/acp-13-10859-2013, 2013.

Kirner, O., Müller, R., Ruhnke, R., and Fischer, H.: Contribution of liquid, NAT and ice particles to chlorine activation and ozone depletion in Antarctic winter and spring, Atmos. Chem. Phys., 15, 2019–2030, doi:10.5194/acp-15-2019-2015, 2015.

Kullmann, A., Riese, M., Olschewski, F., Stroh, F., and Grossmann, K. U.: Cryogenic infrared spectrometers and telescopes for the atmosphere – new Frontiers, Proc. SPIE, 5570, 423–432, 2004.

Lowe, D., and MacKenzie, A.R.: Polar stratospheric cloud microphysics and chemistry, J. Atmos. Sol.-Terr. Phys., 70, 13–40,doi:10.1016/j.jastp.2007.09.011, 2008.

Marshall, B.T., Gordley, L.L., and Chu, D.A.: BANDPAK: Algorithms for Modeling Broadband Transmission and Radiance, J. Quant. Spectrosc. Radiat. Transfer, 52, 581–599, 1994.

Molleker, S., Borrmann, S., Schlager, H., Luo, B., Frey, W., Klingebiel, M., Weigel, R., Ebert, M., Mitev, V., Matthey, R., Woiwode, W., Oelhaf, H., Dörnbrack, A., Stratmann, G., Grooß, J.-U., Günther, G., Vogel, B., Müller, R., Krämer, M., Meyer, J.,and Cairo, F.: Microphysical properties of synoptic-scale polarstratospheric clouds: in situ measurements of unexpectedly large HNO_3-containing particles in the Arctic vortex, Atmos. Chem.Phys., 14, 10785–10801, doi:10.5194/acp-14-10785-2014, 2014.

Offermann, D., Grossmann, K.-U., Barthol, P., Knieling, P., Riese, M., and Trant, R.: Cryogenic Infrared Spectrometers and Telescopes for the Atmosphere (CRISTA) experiment and middle atmosphere variability, J. Geophys. Res., 104, 16311–16325, doi:10.1029/1998JD100047, 1999.

Orr, A., Hosking, J. S., Hoffmann, L., Keeble, J., Dean, S. M., Roscoe, H. K., Abraham, N. L., Vosper, S., and Braesicke, P.: Inclusion of mountain-wave-induced cooling for the formation of PSCs over the Antarctic Peninsula in a chemistry-climate model, Atmos. Chem. Phys., 15, 1071–1086, 10.5194/acp-15-1071-2015, 2015.

Peter, T. and Grooß, J.-U.: Polar Stratospheric Clouds and Sulfate Aerosol Particles: Microphysics, Denitrification and Heterogeneous Chemistry, in: Stratospheric Ozone Depletion and Climate Change, edited by Müller, R., Royal Society of Chemistry, 2012.

Pitts, M.C., Poole, L.R., and Gonzalez, R.: Polar stratospheric cloud climatology based on CALIPSO spaceborne lidar measurements from 2006 to 2017, Atmos. Chem. Phys., 18, 10881–10913, 10.5194/acp-18-10881-2018, 2018.

Pope, R.J., Richards, N.A.D., Chipperfield, M.P., Moore, D.P., Monks, S.A., Arnold, S.R., Glatthor, N., Kiefer, M., Breider, T.J., Harrison, J.J., Remedios, J.J., Warneke, C., Roberts, J.M., Diskin, G.S., Huey, L.G., Wisthaler, A., Apel, E.C., Bernath, P.F., and Feng, W.:

Intercomparison and evaluation of satellite peroxyacetyl nitrate observations in the upper troposphere–lower stratosphere, Atmos. Chem. Phys., 16, 13541–13559, doi:10.5194/acp-16-13541-2016, 2016.

Preusse, P., Schroeder, S., Hoffmann, L., Ern, M., Friedl-Vallon, F., Ungermann, J., Oelhaf, H., Fischer, H., and Riese, M.: New perspectives on gravity wave remote sensing by spaceborne infrared limb imaging, Atmos. Meas. Tech., 2, 299–311, 2009.

Remedios, J.J., Leigh, R.J., Waterfall, A.M., Moore, D.P., Sembhi, H., Parkes, I., Greenhough, J., Chipperfield, M.P., and Hauglustaine, D.: MIPAS reference atmospheres and comparisons to V4.61/V4.62 MIPAS level 2 geophysical data sets, Atmos. Chem. Phys. Discuss., 7, 9973–10017, doi:10.5194/acpd-7-9973-2007, 2007.

Riediger, O., Volk, C. M., Strunk, M., and Schmidt, U.: HAGAR – a new in situ tracer instrument for stratospheric balloons and high altitude aircraft, Eur. Comm. Air Pollut. Res. Report, 73, 727–730, 2000.

Riese, M., Oelhaf, H., Preusse, P., Blank, J., Ern, M., Friedl-Vallon, F., Fischer, H., Guggenmoser, T., Höpfner, M., Hoor, P., Kaufmann, M., Orphal, J., Plöger, F., Spang, R., Suminska-Ebersoldt, O., Ungermann, J., Vogel, B., and Woiwode, W.: Gimballed Limb Observer for Radiance Imaging of the Atmosphere (GLORIA) scientific objectives, Atmos. Meas. Tech., 7, 1915–1928,doi:10.5194/amt-7-1915-2014, 2014.

Schroeder, S., Kullman, A., Preusse, P., Stroh, F., Weigel, K., Ern, M., Knieling, P., Olschewski, F., Spang, R., and Riese, M.: Radiance calibration of CRISTA-NF, Adv. Space Res., 43, 1910–1917, doi:10.1016/j.asr.2009.03.009, 2009.

Solomon, S.: Stratospheric ozone depletion: A review of concepts and history, Rev. Geophys., 37, 275–315, 1999.

Solomon, S., Kinnison, D., Bandoro, J., and Garcia, R.: Simulation of polar ozone depletion: An update, J. Geophys. Res.-Atmos., 120, 7958–7974, doi:10.1002/2015JD023365, 2015.

Spang, R., Riese, M., and Offermann, D.: CRISTA-2 observations of the south polar vortex in winter 1997: A new dataset for polar process studies, Geophys. Res. Lett., 25, 3159–3162, doi:10.1029/2000GL012374, 2001.

Spang, R., Eidmann, G., Riese, M., Offermann, D., and Preusse, P: CRISTA observations of cirrus clouds around the tropopause, J. Geophys. Res., 107, D23, doi:10.1029/2001JD000698, 2002.

Spang, R., and Remedios, J.J.: Observations of a distinctive infra-red spectral feature in the atmospheric spectra of polar stratospheric clouds measured by the CRISTA instrument, Geophys. Res. Lett., 30, 1875, doi:10.1029/2003GL017231, 2003.

Spang, R., Remedios, J.J., Kramer, L.J., Poole, L.R., Fromm, M.D., Müller, M., Baumgarten, G., and Konopka, P.: Polar stratospheric cloud observations by MIPAS on ENVISAT: detection method, validation and analysis of the northern hemisphere winter 2002/2003, Atmos. Chem. Phys., 5, 679–692, doi:10.5194/acp-5-679-2005, 2005.

Spang, R., Hoffmann, L., Kullmann, A., Olschewski, F., Preusse, P., Knieling, P., Schroeder, S., Stroh, F., Weigel, K., and Riese, M.: High resolution limb observations of clouds by the CRISTA-NF experiment during the SCOUT-O3 tropical aircraft campaign, Adv. Space Res., 42, 1765–1775, doi:10.1016/j.asr.2007.09.036, 2008.

Spang, R., Arndt, K., Dudhia, A., Höpfner, M., Hoffmann, L., Hurley, J., Grainger, R.G., Griessbach, S., Poulsen, C., Remedios, J.J., Riese, M., Sembhi, H., Siddans, R., Waterfall, A., and Zehner, C.: Fast cloud parameter retrievals of MIPAS/Envisat, Atmos. Chem. Phys., 12, 7135-7164, doi:10.5194/acp-12-7135-2012, 2012.

Spang, R., Günther, G., Riese, M., Hoffmann, L., Müller, R., and Griessbach, S.: Satellite observations of cirrus clouds in the Northern Hemisphere lowermost stratosphere, Atmos. Chem. Phys., 15, 927-950, doi:10.5194/acp-15-927-2015, 2015.

Spang, R., Hoffmann, L., Höpfner, M., Griessbach, S., Müller, R., Pitts, M.C., Orr, A.M.W., and Riese, M.: A multi-wavelength classification method for polar stratospheric cloud types using infrared limb spectra, Atmos. Meas. Tech., 9, 3619-3639, doi:10.5194/amt-9-3619-2016, 2016.

Spang, R., Hoffmann, L., Müller, R., Grooß, J.-U., Tritscher, I., Höpfner, M., Pitts, M., Orr, A., and Riese, M.: A climatology of polar stratospheric cloud composition between 2002 and 2012 based on MIPAS/Envisat observations, Atmos. Chem. Phys., 18, 5089-5113, doi:10.5194/acp-18-5089-2018, 2018.

Toon, O.B., Tolbert, M.A., Koehler, B.G., Middlebrook, A.M., and Jordan, J.: Infrared optical constants of H2O ice, amorphous nitric acid solutions, and nitric acid hydrates, J. Geophys. Res., 99(D12), 25631–25654, doi:10.1029/94JD02388, 1994.

Tritscher, I., Pitts, M.C., Poole, L.R., Alexander, S.P., Cairo, F., Chipperfield, M.P., Grooß, J.-U., Höpfner, M., Lambert, A., Luo, B.P, Molleker, S., Orr, A., Salawitch, R., Snels, M., Spang, R., Woiwode, W., and Peter, T.: Polar Stratospheric Clouds: Observations, Processes, and Role in Ozone Depletion, currently under review for Rev. Geophys., 2020.

Ungermann, J., Kalicinsky, C., Olschewski, F., Knieling, P., Hoffmann, L., Blank, J., Woiwode, W., Oelhaf, H., Hösen, E., Volk, C. M., Ulanovsky, A., Ravegnani, F., Weigel, K., Stroh, F., and Riese, M.: CRISTA-NF measurements with unprecedented vertical resolution during the RECONCILE aircraft campaign, Atmos. Meas. Tech., 5, 1173–1191, doi:10.5194/amt-5-1173-2012, 2012.

von Hobe, M., Bekki, S., Borrmann, S., Cairo, F., D'Amato, F., Di Donfrancesco, G., Dörnbrack, A., Ebersoldt, A., Ebert, M., Emde, C., Engel, I., Ern, M., Frey, W., Genco, S., Griessbach, S., Grooß, J.-U., Gulde, T., Günther, G., Hösen, E., Hoffmann, L., Homonnai, V., Hoyle, C. R., Isaksen, I. S. A., Jackson, D. R., Jánosi, I. M., Jones, R. L., Kandler, K., Kalicinsky, C., Keil, A., Khaykin, S. M., Khosrawi, F., Kivi, R., Kuttippurath, J., Laube, J. C., Lefèvre, F., Lehmann, R., Ludmann, S., Luo, B. P., Marchand, M., Meyer, J., Mitev, V., Molleker, S., Müller, R., Oelhaf, H., Olschewski, F., Orsolini, Y., Peter, T., Pfeilsticker, K., Piesch, C., Pitts, M. C., Poole, L. R., Pope, F. D., Ravegnani, F., Rex, M., Riese, M., Röckmann, T., Rognerud, B., Roiger, A., Rolf, C., Santee, M. L., Scheibe, M., Schiller, C., Schlager, H., Siciliani de Cumis, M., Sitnikov, N., Søvde, O. A., Spang, R., Spelten, N., Stordal, F., Sumińska-Ebersoldt, O., Ulanovski, A., Ungermann, J., Viciani, S., Volk, C. M., vom Scheidt, M., von der Gathen, P., Walker, K., Wegner, T., Weigel, R., Weinbruch, S., Wetzel, G., Wienhold, F. G., Wohltmann, I., Woiwode, W., Young, I. A. K., Yushkov, V., Zobrist, B., and Stroh, F.: Reconciliation of essential process parameters for an enhanced predictability of Arctic stratospheric ozone loss and its climate interactions (RECONCILE): activities and results, Atmos. Chem. Phys., 13, 9233–9268, doi:10.5194/acp-13-9233-2013, 2013.

Waibel, A.E., Peter, T., Carslaw, K.S., Oelhaf, H., Wetzel, G., Crutzen, P.J., Pöschl, U., Tsias, A., Reimer, E., and Fischer, H.:Arctic Ozone Loss Due to Denitrification, Science, 283, 2064–2069, doi:10.1126/science.283.5410.2064, 1999.

Wegner, T., Grooß, J.-U., von Hobe, M., Stroh, F., Suminska-Ebersoldt, O., Volk, C. M., Hösen, E., Mitev, V., Shur, G., and Müller, R.: Heterogeneous chlorine activation on stratospheric aerosols and clouds in the Arctic polar vortex, Atmos. Chem. Phys., 12, 11095–11106, doi:10.5194/acp-12-11095-2012, 2012.

Weigel, K.: Infrared limb-emission observations of the upper troposphere, lower stratosphere with high spatial resolution, Ph.D. thesis, University of Wuppertal, Wuppertal, Germany, 2009.

Weigel, K., Riese, R., Hoffmann, L., Hoefer, S., Kalicinsky, C., Knieling, P., Olschewski, F., Preusse, P., Stroh, F., Spang, R., and Volk, C.M.: CRISTA-NF measurements during the AMMA-SCOUT-O3 aircraft campaign, Atmos. Meas. Tech., 3, 1437–1455, 2010.

Werner, A., Volk, C. M., Ivanova, E. V., Wetter, T., Schiller, C.,Schlager, H., and Konopka, P.: Quantifying transport into the Arctic lowermost stratosphere, Atmos. Chem. Phys., 10, 11623–11639, doi:10.5194/acp-10-11623-2010, 2010.

Wohltmann, I., Wegner, T., Müller, R., Lehmann, R., Rex, M., Manney, G. L., Santee, M. L., Bernath, P., Suminska-Ebersoldt, O., Stroh, F., von Hobe, M., Volk, C. M., Hösen, E., Ravegnani, F., Ulanovsky, A., and Yushkov, V.: Uncertainties in modelling heterogeneous chemistry and Arctic ozone depletion in the winter 2009/2010, Atmos. Chem. Phys., 13, 3909–3929,doi:10.5194/acp-13-3909-2013, 2013.

Woiwode, W., Höpfner, M., Bi, L., Pitts, M.C., Poole, L.R., Oelhaf, H., Molleker, S., Borrmann, S., Klingebiel, M., Belyaev, G., Ebersoldt, A., Griessbach, S., Grooß, J.-U., Gulde, T., Krämer, M., Maucher, G., Piesch, C., Rolf, C., Sartorius, C., Spang, R., and Orphal, J.:

Spectroscopic evidence of large aspherical β-NAT particles involved in denitrification in the December 2011 Arctic stratosphere, Atmos. Chem. Phys., 16, 9505-9532, doi:10.5194/acp-16-9505-2016, 2016.

Woiwode, W., Höpfner, M., Bi, L., Khosrawi, F., and Santee, M.L.: Vortex-Wide Detection of Large Aspherical NAT Particles in the Arctic Winter 2011/12 Stratosphere, Geophys. Res. Lett., 46, 13420– 13429, doi:10.1029/2019GL084145, 2019.

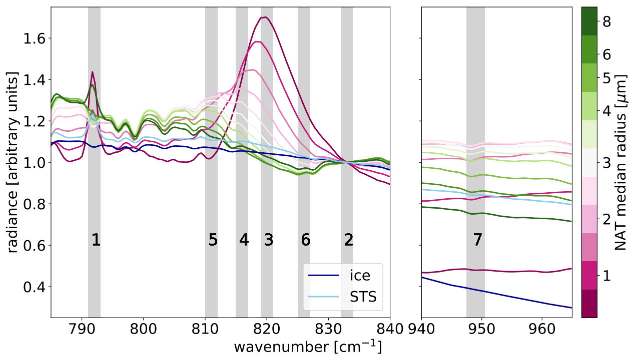

Figure 1. Selected simulation results for infrared spectra in the presence of polar stratospheric clouds consisting of NAT particles with different particle median radii, STS, and ice. The spectra have been scaled using the mean radiance in the spectral window 832.0 – 834.0 cm^{-1} such that the radiance for all spectra equals 1 in ~~the spectral window 832.0 – 834.0 cm^{-1}.~~ this window. The gray vertical bars mark the micro windows (MW) used during the analysis. The are numbered from MW1 to MW7.

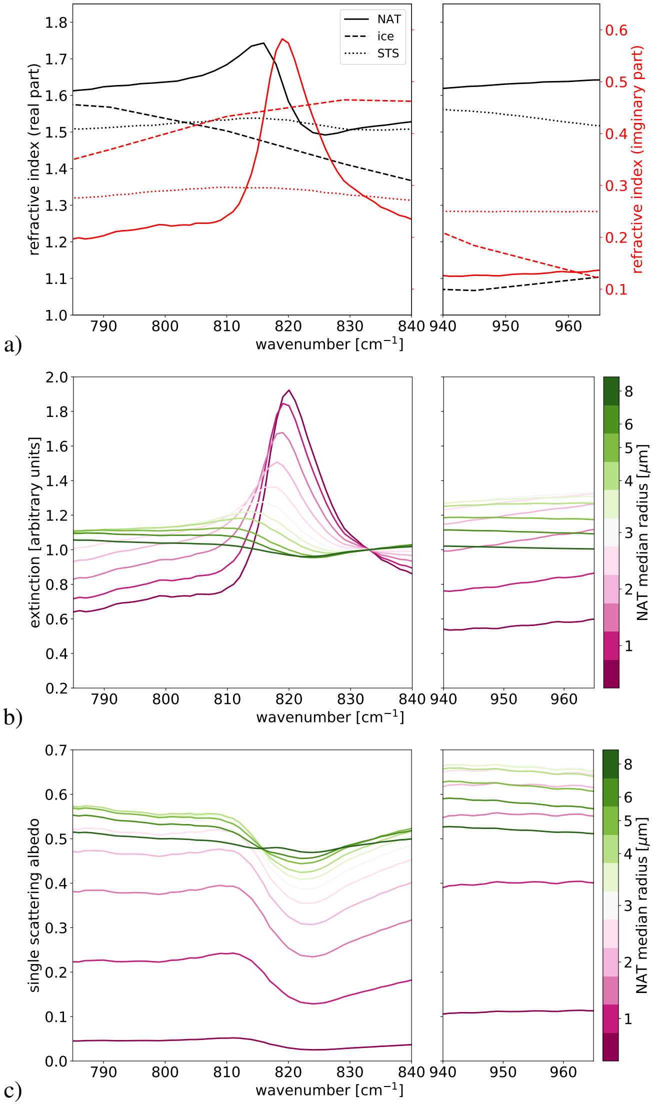

Figure 2. ~~Real and imaginary part of the refractive index of β-NAT by Biermann (1998) with refinement in Höpfner et al (2006)~~ a) Refractive indices for NAT (solid lines), STS (dottes lines), and ice (dashed lines). The real parts are shown in black and the imaginary parts in red with a second axis to the right. The refractive indices for NAT, STS, and ice were taken from Biermann (1998) with refinement in Höpfner et al. (2006), Biermann et al. (2000), and Toon et al. (1994), respectively. b) Extinction spectra for NAT with different median radii. The spectra have been scaled using the mean value in the spectral window 832.0 – 834.0 cm^{-1} such that the extinction for all spectra equals 1 in this window. c) Single scattering albedo for NAT with different median radii.

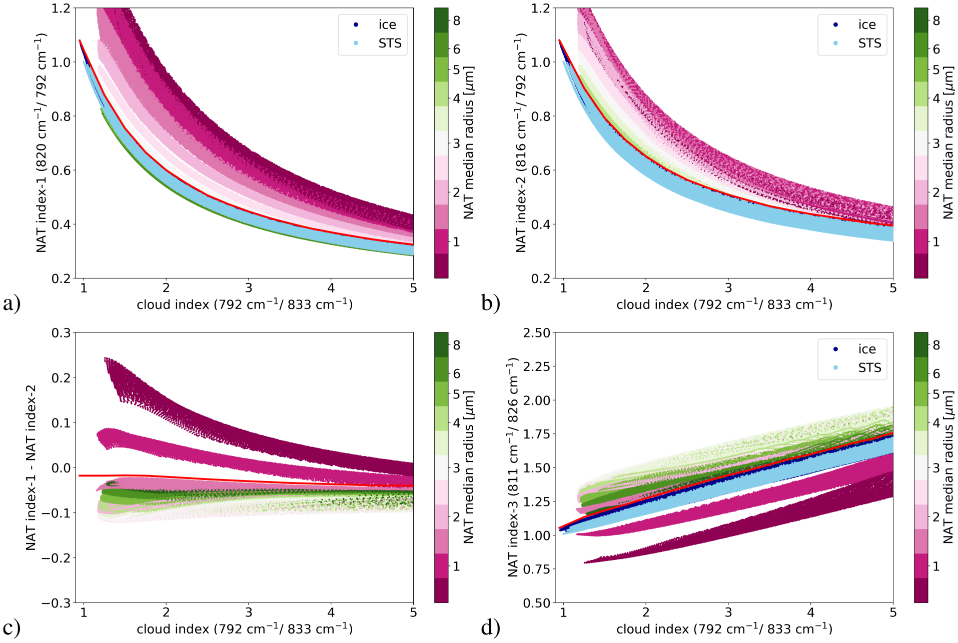

Figure 3. Scatter plots for different NAT indices versus cloud index. a) NAT index-1 (819 – 821 cm^{-1})/(791 – 793 cm^{-1}); b) NAT index-2 (815 – 817 cm^{-1})/(791 – 793 cm^{-1}); c) NAT index-1 – NAT index-2; d) NAT index-3 (810 – 812 cm^{-1})/(825 – 827 cm^{-1}). The ~~black~~ red lines show the separation lines, which mark the upper envelope of the regions of STS and ice (in a), b), and d)) or the region of medium and large NAT (in c)). Simulation results for ice and STS are in shown in dark and light blue, respectively.

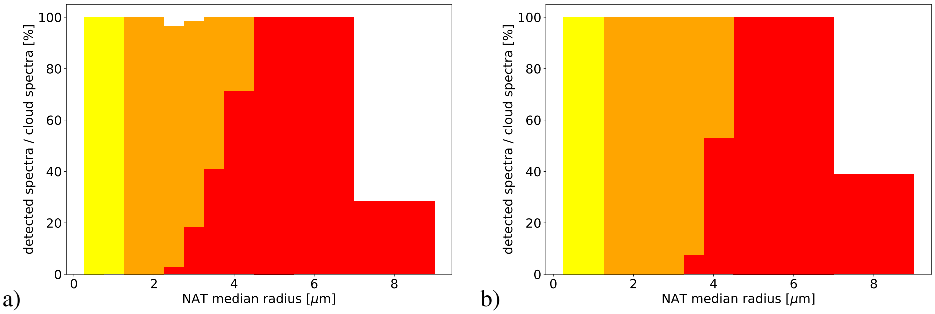

Figure 4. The histograms ~~show~~ of the proportion of the detected spectra (NAT) per simulated cloud spectra in each size bin ~~of the simulations~~. The colours illustrate the different cases 1 – 3. Case-1 (sNAT) is shown in yellow, case-2 (mNAT) in orange, case-3 (lNAT) in red. For the description of the different cases see details in text. In panel a) the CI threshold value to detect a spectrum as cloud spectrum is 5.0 (in total about 365000 cloud spectra) and in panel b) 3.0 (in total about 197000 cloud spectra).

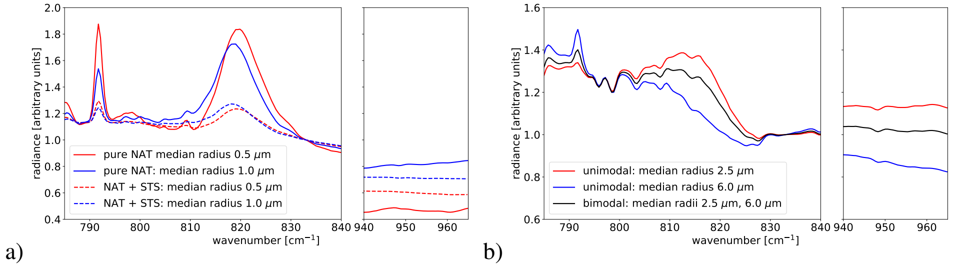

Figure 5. Selected spectra for NAT/STS mixed clouds (a)) and bimodal NAT particle size distributions (b)). The spectra were scaled using the mean radiance in the spectral window 832.0 – 834.0 cm^{-1} such that the radiance for all spectra equals 1 in ~~the spectral window 832.0 – 834.0 cm^{-1}.~~ this window. a) The solid lines show spectra for unimodal NAT particle size distributions. Red: median radius 0.5 µm and 10 ppbv HNO_3; Blue: median radius 1.0 µm and 10 ppbv HNO_3. The dashed lines show the NAT/STS mixed clouds. The amount of NAT is the same as for the pure NAT simulations and the volume density of STS is 10 µm^3/cm^3 in both cases. b) The red and blue lines show the spectra for unimodal size distributions with median radius 2.5 µm and 6.0 µm, respectivley. The amount of HNO_3 is 10 ppbv in each case. The black line shows the simulation results for a bimodal size distribution with the median radii 2.5 µm and 6.0 µm and 5 ppbv HNO_3 in each mode.

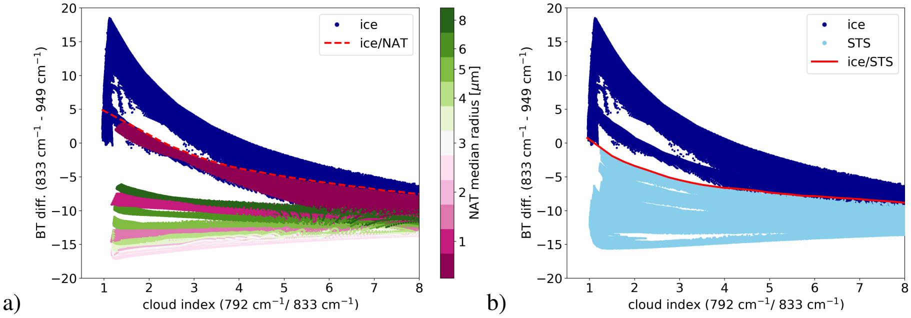

Figure 6. Scatter plots for BT difference (832 – 834 cm^{-1}) – (947.5 – 950.5 cm^{-1}) versus cloud index. The red solid line shows the separation line between ice and STS and the dashed line marks the separation between ice and NAT.

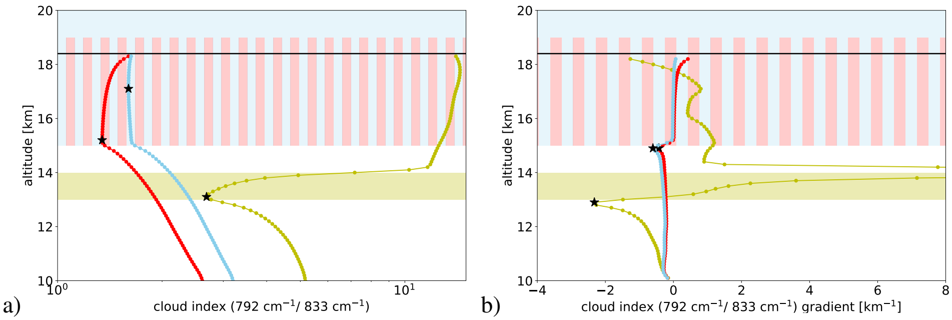

Figure 7. Vertical profiles of the cloud index (left) and the vertical gradient of the cloud index (right) for clouds with different vertical thicknesses. The colour coding shows the vertical thickness (yellow: 1 km, red: 4 km, light blue: 8 km up to 23 km). The HNO_3 VMRs inside the NAT PSCs are 5 ppbv for the 1 and 8 km thick clouds and 10 ppbv for the 4 km thick cloud. The corresponding shaded areas illustrate the vertical extent of the clouds. The black stars mark the altitudes of the CI minima and the CI gradient minima. The black horizontal line shows the flight altitude.

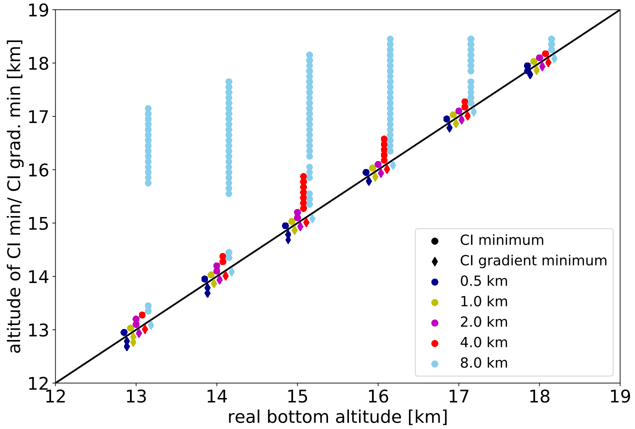

Figure 8. Altitude of CI minimum (full circles) and CI gradient minimum (full diamonds) against the real bottom altitude. The black line shows the line with slope 1. The different cloud thicknesses are shown colour coded and the points have been shifted along the line for clearness. Clouds with a CI minimum < 1.2 (optically thick) and > 5.0 (optically thin) have been excluded.

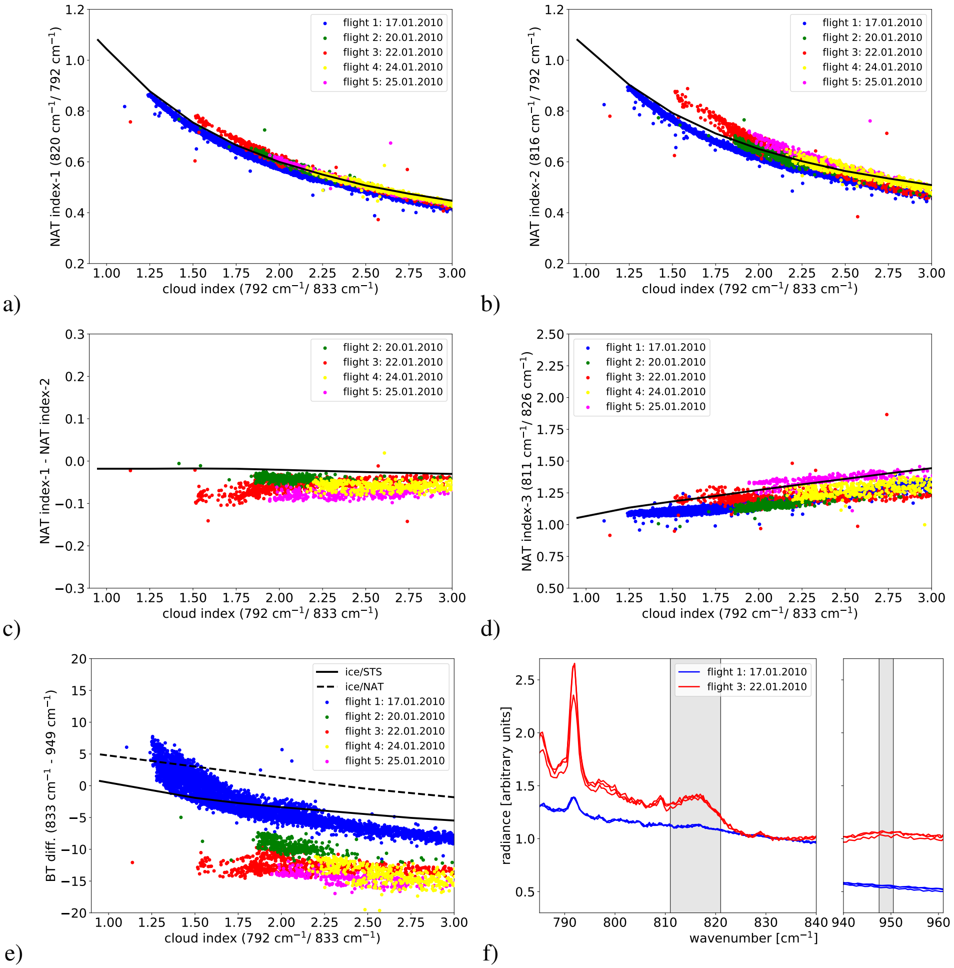

Figure 9. Scatter plots for different NAT indices versus cloud index for the CRISTA-NF observations during RECONCILE flights 1 – 5. a) NAT index-1 (819 – 821 cm^{-1})/(791 – 793 cm^{-1}) (MW3/MW1); b) NAT index-2 (815 – 817 cm^{-1})/(791 – 793 cm^{-1}) (MW4/MW1); c) NAT index-1 – NAT index-2; d) NAT index-3 (810 – 812 cm^{-1})/(825 – 827 cm^{-1}) (MW5/MW6). The black lines show the separation lines, which mark the upper envelope of the regions of STS and ice (in a), b), and d)) or the region of medium and large NAT (in c)). Simulation results for ice and STS are in shown in dark and light blue, respectively. e) Scatter plot for BT difference (832 – 834 cm^{-1}) – (947.5 – 950.5 cm^{-1}) versus cloud index for the CRISTA-NF observations during RECONCILE flights 1 – 5. The black solid line shows the separation line between ice and STS and the dashed line marks the separation between ice and NAT. f) Example spectra from flight 1 and flight 3. The spectra have been scaled such that the radiance for all spectra equals 1 in the spectral window 832.0 – 834.0 cm^{-1}. The gray bar marks the region of the shifted NAT feature and the region used for the BTD around 949 cm^{-1}.

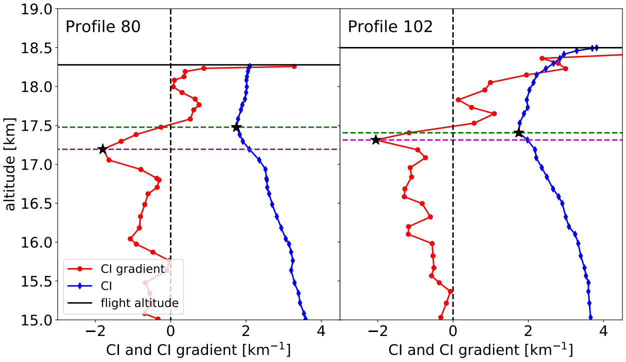

Figure 10. Altitude profiles of the cloud index (CI) and the CI gradient for two selected profiles of the CRISTA-NF measurements during RECONCILE flight 3. The CI is shown as a blue curve and the CI gradient as red curve. The flight altitude is marked by a horizontal black line. The dashed green and magenta lines show the minima of the CI and CI gradient profile, respectively.

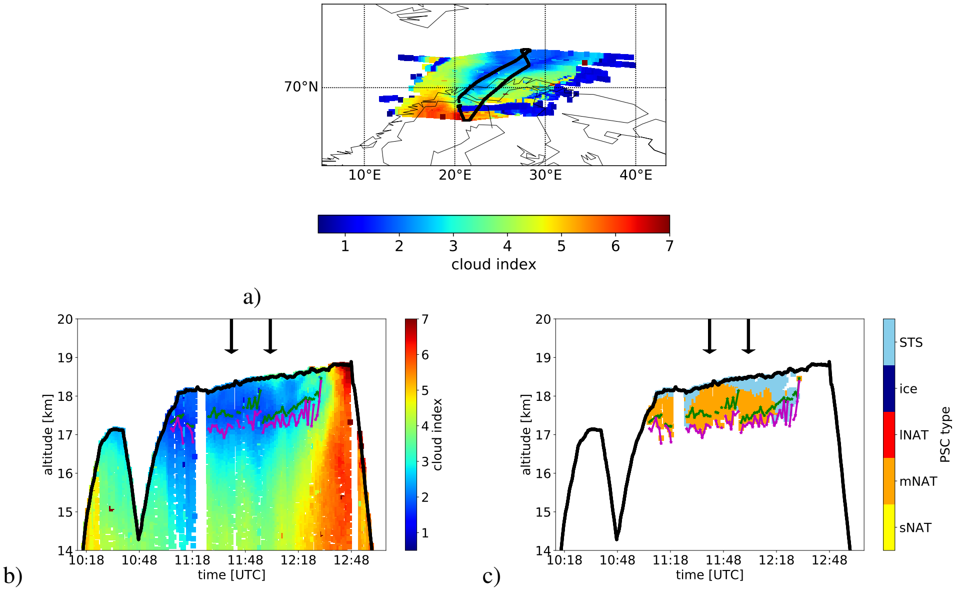

Figure 11. ~~a) Cross section plot of the cloud index for RECONCILE flight 3. b) Cross section plot of the PSC types.~~a), b) Longitude-latitude and cross section plot of the cloud index for RECONCILE flight 3. c) Cross section plot of the PSC types. The analysis of the PSC composition was performed for all spectra between flight altitude and CI gradient minimum. The black line shows the flight altitude of the aircraft. The CI minimum and the CI gradient minimum are marked by a green and a magenta line, respectively. Only profiles with a CI minimum below 3.0 and where both minima can sufficently by determined are considered. The black arrows in b) and c) mark the two profiles shown in Fig. 10.

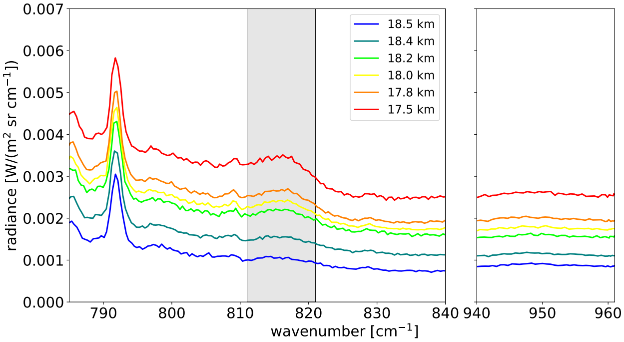

Figure 12. Example infrared spectra measured by CRISTA-NF during RECONCILE flight 3 inside PSCs at about 12:10 UTC. The spectra at different tangent altitudes are shown colour coded. The gray bar marks the region of the shifted NAT feature.

Table 1. ~~Simulation properties with respect to the viewing geometry and the spectral properties~~ CRISTA-NF instrument properties used in the simulations

property	value
vertical sampling	100 m
spectral sampling	0.42 cm^{-1} for 785 – 840 cm^{-1}
	0.59 cm^{-1} for 940 – 965 cm^{-1}
spectral resolving power $\frac{\lambda}{\Delta\lambda}$	536 at 12.5 µm
observer altitude	18.4 km
altitude range	10 km – observer altitude

Table 2. ~~Simulation properties with respect to background atmosphere~~ Setup of the background atmosphere for the simulations

constituent	source	spectral region
temperature	ERA-Interim (Dee et al., 2011)	both
pressure	ERA-Interim (Dee et al., 2011)	both
CO_2	Diallo et al. (2017)	both
HNO_3	climatology	both
O_3	climatology	both
$ClONO_2$	climatology	785–840 cm^{-1}
H_2O	climatology	both
HNO_4	climatology	785–840 cm^{-1}
CCl_4	climatology	785–840 cm^{-1}
ClO	climatology	785–840 cm^{-1}
NO_2	climatology	785–840 cm^{-1}
CFC-11	climatology with update (using HAGAR (Riediger et al., 2000; Werner et al., 2010) and Bullister (2011))	both
HCFC-22	climatology with update (using ACE-FTS (Boone et al., 2013))	785–840 cm^{-1}
CFC-113	climatology with update (using Bullister (2011))	785–840 cm^{-1}
PAN	CRISTA-NF	both
SF_6	climatology with update (using ACE-FTS (Boone et al., 2013))	940–965 cm^{-1}
NH_3	climatology	940–965 cm^{-1}
COF_2	climatology with update (using ACE-FTS (Boone et al., 2013) and Bullister (2011))	940–965 cm^{-1}

Table 3. Cloud scenario simulation setup

cloud dimension	values
PSC position	13.0 – 30.0 km
PSC thickness	0.5, 1.0, 2.0, 4.0, 8.0 km

PSC type	HNO_3 VMR [ppbv]* / volume density [µm^3/cm^3]**	radius [µm]	extinction [km^{-1}]
NAT	1 – 15*	0.5, 1.0, 1.5, 2.0, 2.5, 3.0, 3.5, 4.0, 5.0, 6.0, 8.0	3.4e^{-5} – 2.2e^{-3}
bimodal NAT	3/7, 5/5, 7/3* (1st/2nd mode)	1st mode: 0.5 – 2.5 2nd mode: larger than in 1st mode	4.4e^{-4} – 1.4e^{-3}
STS with wt% H_2SO_4/HNO_3 2/48, 25/25, and 48/2	0.1, 0.5, 1.0, 5.0, 10.0**	0.1, 0.3, 0.5, 1.0	2.1e^{-5} – 4.1e^{-3}
NAT + STS wt% 2/48	NAT: 5, 10, 15* STS: 5.0, 10.0**	NAT: 0.5 – 3.5 STS: 0.1, 0.3, 1.0	5e^{-4} – 3.5e^{-3}
ice	0.1, 0.5, 1.0, 5.0, 10.0, 50.0, 100.0**	1.0, 2.0, 3.0, 4.0, 5.0, 10.0	1.0e^{-5} – 1.0e^{-2}

Table 4. Summary of the indices and their corresponding micro windows.

name of index	definition	definition with short names
cloud index CI	(791 – 793 cm^{-1})/(832 – 834 cm^{-1})	(MW1)/(MW2)
NAT index-1	(819 – 821 cm^{-1})/(791 – 793 cm^{-1})	(MW3)/(MW1)
NAT index-2	(815 – 817 cm^{-1})/(791 – 793 cm^{-1})	(MW4)/(MW1)
NAT index-3	(810 – 812 cm^{-1})/(825 – 827 cm^{-1})	(MW5)/(MW6)
BTD	BT(832 – 834 cm^{-1}) - BT(947.5 – 950.5 cm^{-1})	BT(MW2) - BT(MW7)